Experimentelle Physik

Position Resolution and Zero Suppression of the ALICE TRD

Diplomarbeit

von

Elke Svenja Wulff

Westfälische Wilhelms-Universität Münster
Institut für Kernphysik

— Februar 2009 —

Contents

CHAPTER 1

Introduction

In September 2008, when the Large Hadron Collider (LHC) at CERN[1] started operating, it aroused the interest of media all over the world. The cost of more than three billion Euro is carried by its 20 member states[2] to find the answers to the old but still open questions, what are we made of and where do we come from. The essential idea of the Big Bang Model is that the universe is expanding from an extremely dense and hot initial condition, starting at some finite time in the past. And whereas today quarks and gluons always bind together to hadrons like neutrons and protons, in the first moments after the Big Bang these fundamental particles, of which existing matter is made of, are expected to appear as free particles, in the so-called 'Quark-Gluon-Plasma' (QGP). The phase transition from the partonic medium to the hadronic phase took place 10^{-5} s after the Big Bang. To learn more about the first moments of our universe before the hadronisation happened, several experiments like RHIC [3] and SPS [4] have been carried out, in which particles are brought to collision at high energies to probe the conditions of extremely high temperatures and pressures right after the Big Bang. Multiple indications have been seen, but up to now no unambiguous evidence for the existence of the QGP could be found in the laboratory. To consolidate the evidence is the goal of A Large Ion Collider Experiment (ALICE) at the LHC. ALICE consists of several different detectors for different tasks. In this diploma thesis the performance of the Transition Radiation Detector (TRD) will be investigated. The position resolution will be determined and parameters for online position reconstruction will be calculated. Since the TRD reaches data rates of 1.1 $\frac{\text{GB}}{\text{s}}$ the huge resulting amount

[1] European Organization for Nuclear Research

[2] Austria, Belgium, Bulgaria, the Czech Republic, Denmark, Finland, France, Germany, Greece, Hungary, Italy, the Netherlands, Norway, Poland, Portugal, the Slovak Republic, Spain, Sweden, Switzerland and the United Kingdom

[3] Relativistic Heavy Ion Collider, BNL (Brookhaven)

[4] Super Proton Synchrotron, CERN (Geneva)

of data has to be stored at several places. To deal conscientiously with the available storage capacity is the important goal of the zero suppression. Thresholds for the data readout that cut out the noise with smallest possible signal loss and no significant effect on the position resolution performance are determined.

CHAPTER 2

Theory

2.1 Standard Model of Particle Physics

The Standard Model of particle physics is the theory of the elementary particles and three of the four known fundamental interactions between them. The constituents of matter are six quarks and six leptons appearing in three different families (see table 2.1).

The three known fundamental forces described by the Standard Model are the weak nuclear force, the strong nuclear force and the electromagnetic force. The fourth one is gravitation. It is postulated that gravitation is mediated by the exchange of a particle similar to the other three forces (see table 2.2). These exchanged particles are called gauge bosons. Bosons are particles with integer spin and thus obey to Bose-Einstein statistics.

Quarks and leptons are fermions which are particles with half-integer spin and thus obey Fermi-Dirac statistics. The leptons interact weakly and, in case they are charged, electro-

	Quarks			**Leptons**		
Family	Name	Charge	Mass	Name	Charge	Mass
1	u	2/3 e	1.5 - 4 MeV/c^2	e^-	-e	0.511 MeV/c^2
	d	-1/3 e	4 - 8 MeV/c^2	ν_e	0	$\leq$ 8 MeV/c^2
2	c	2/3 e	1.15 - 1.35 GeV/c^2	μ^-	-e	105 MeV/c^2
	s	-1/3 e	80 - 130 MeV/c^2	ν_μ	0	$\leq$ 0.19 MeV/c^2
3	t	2/3 e	174.3 $\pm$ 5.1 GeV/c^2	τ^-	-e	1.78 GeV/c^2
	b	-1/3 e	4.1 - 4.4 GeV/c^2	ν_τ	0	$\leq$ 18.2 GeV/c^2

Table 2.1: The Standard Model: The constituents of matter are the quarks and leptons [A$^+$08].

Force	Relative Strength	Gauge Bosons	Acts on
Strong nuclear force	1	Gluons	Quarks
Electromagnetic force	$\frac{1}{137}$	Photons	All charged particles
Weak nuclear force	$\sim 10^{-7}$	$W^{\pm}, Z^0$	Quarks, leptons
Gravitation	$\sim 10^{-39}$	Gravitons	All massive particles

Table 2.2: The Standard Model: Fundamental forces. The strong nuclear force acts on the colour charge (*red,* $\overline{red}$*, green,* $\overline{green}$*, blue* or $\overline{blue}$) of the quarks like the electromagnetic force acts on charge. The gravitation is the only fundamental force that is not described by the standard model [Per00].

magnetically . They appear as free particles, whereas quarks never appear as free particles. Quarks also interact weakly and electromagnetically like leptons and in addition, the strong force acts on the colour charge of the quarks. This interaction among quarks is mediated by eight gauge bosons, the gluons. It is described by Quantum Chromodynamics (QCD), the quantum field theory of the strong interaction.
The strong force differs from all other fundamental forces since its strength increases with greater distance between two interacting quarks and weakens if the quarks get closer to one another. The potential between two quarks can be approximated by [Sat90]:

$$V(r) = -\frac{\alpha}{r} + \sigma r \tag{2.1}$$

The first term is similar to the Coulomb potential whereas the second positive one describes the long range behaviour of the strong nuclear force. As a conclusion the QCD predicts two particular properties of the strong force called '*asymptotic freedom*' and '*confinement*'. The former describes the effect that quarks and gluons interact very weakly if they get close to each other as for example in high-energy reactions with large momentum transfer. The latter corresponds to the circumstance that an infinite amount of energy is necessary to seperate two quarks because the strength of the interaction increases with larger distance between them. Thus quarks and gluons do not occur as free particles but always bind together to hadrons.
Therefrom, today the world is made of hadronic matter. Quarks and gluons are confined to the size of two different kinds of hadrons. The first ones are called baryons. They are formed out of three quarks and are fermions. The proton, which is made of two up and one down quark (uud), and the neutron (udd) are examples for baryons. The combination of three antiquarks is also possible and is called an antibaryon.
The second kind are the mesons. They are composed of two quarks and thus are bosons. Examples for mesons are the charged pions π^+ ($u\overline{d}$) and π^- ($\overline{u}d$). Mesons always consist of a quark and an antiquark. In one hadron the colours always have to combine to colourless (white), analogous to the behaviour of the primary colours. In the case of a

baryon the colours have to be red, blue and green or $\overline{\text{red}}$, $\overline{\text{blue}}$ and $\overline{\text{green}}$, whereas in a meson any colour in combination with its anticolour is possible.
The goal of the ALICE experiment is to find a new state of matter − the *Quark-Gluon Plasma* (QGP) − where the strongly interacting quarks and gluons become free and are not longer confined in hadrons. The temperatures and densities reached in the collisions at the LHC are expected to transform nuclear matter into this new deconfined phase, which existed during the very first moments of our universe.

2.2 Quark-Gluon Plasma

At the LHC heavy ions will collide with a center-of-mass energy up to 1150 TeV in lead-lead collisions. This corresponds to a center-of-mass energy per colliding nucleon pair of $\sqrt{s_{NN}} = 5.5\,\text{TeV}$. It is expected that this energy is high enough for quarks and gluons to become deconfined and move freely forming a new kind of matter. Solving the QCD on a space-time lattice results in a critical temperature T_C for this phase transition of $173\,\text{MeV} \pm 10\,\%$[1] [BMS07]. The outcome is calculated for a vanishing chemical potential μ_B. This corresponds to a zero net baryon density where no difference between baryon and antibaryon densities exists. With increasing chemical potential the transition temperature drops (see illustration 2.1). The dashed line up to a so-called critical point denotes the region where no first order phase transition is possible. A first order phase transition exhibits a discontinuity in the first derivative of the free energy ($\partial F/\partial T$) but no discontinuity in the lower derivatives in T [Won94]. Beyond the critical point no discontinuity occurs.
The QCD predicts conservation for right-handed and left-handed quarks separately ('chiral symmetry') but due to the finite quark masses the chiral symmetry is broken in confined matter, where only the overall baryion number is conserved. The QGP is expected to sustain the chiral symmetry.

To form a plasma the deconfined particles have to be in local equilibrium, otherwise they do not behave like matter but like individual particles. In that case thermodynamic variables like temperature are not defined and there are no thermodynamic phases. To achieve the local equilibrium, the lifetime of the system must be at least about five orders of magnitude larger than the inverse rate of interactions. In chapter (3.1 − 'The LHC') the expected 'canonical' formation time, lifetime and other parameters of the system at LHC energies are discribed.

In figure 2.2 the temporal evolution of a QGP after a collision between two heavy nuclei is demonstrated. The colliding nuclei are Lorentz-contracted in the laboratory frame

[1] In kT units all temperatures are multiplied by Boltzmann's constant $k = 8.417 \times 10^{-5}$ eV K^{-1}

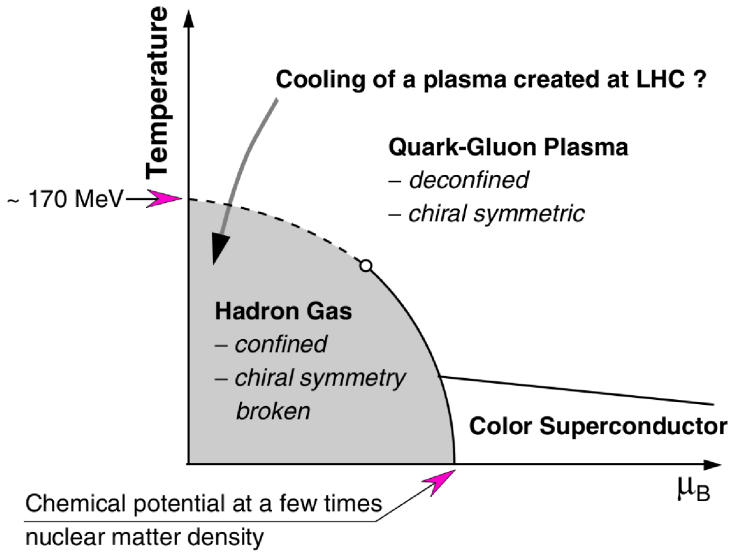

Figure 2.1: Scheme of the QCD phase diagram of nuclear matter in terms of the temperature (T) and chemical potential (μ_B) [ppr04].

due to their ultra-relativistic velocity (figure 2.2 a). When the two nuclei are brought to collision and penetrate each other, direct scattering between their quarks and gluons occurs and the nucleons break up into their components (figure 2.2 b). The fireball emerging from the collision is expected to exceed the critical temperature and to contain tens of thousands of interacting gluons and quarks so that a QGP is formed (figure 2.2 c). Due to expansion the QGP cools down and the quarks recombine to hadrons and mesons (*hadronization*)(figure 2.2 d). After the so-called *chemical freeze out* no free quarks or gluons are left. There are still elastic interactions between the produced particles until the so called *thermal freeze out*.

In the first phase of the collision (figure 2.2 b) pairs of quarks and gluons may scatter back-to-back. The scattered particles break up into jets of other particles, like pions and kaons, which can be seen in the detector later. But before they break up, the scattered quarks and gluons have to move through the region of the emerging fireball. If there is a dense nuclear matter created, the quarks and gluons lose energy on their way through it so that the measured energy of the corresponding jet is decreased as well. Some of them may lose that much energy that their resulting jets can not be detected at all. This effect is called 'jet quenching' [HM96]. It is a signature of the QGP and a strong indication of the new state of matter.
A second signature of the QGP is the so-called J/ψ suppression or enhancement. The J/ψ is the ground state of the *charmonium* ($c\bar{c}$). The first excited state of the charmonium

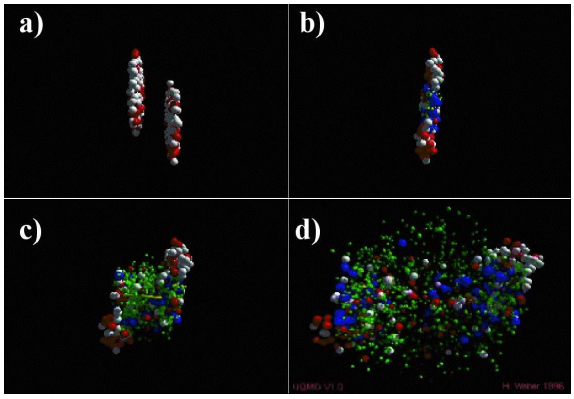

Figure 2.2: Simulation of a collision between two heavy nuclei. The two nuclei appear as two thin discs in the laboratory frame because they are Lorentz-contracted (a). During the collision direct scattering of quarks and gluons happens (b). In the region where the collision has been taken place the energy density is expected to be high enough, that a QGP is formed (c). The QGP cools down and the quarks recombine to hadrons (*hadronization*)(d) [Web].

is called ψ'. The decay of both states is supressed ('narrow states') due to the need of changing quark flavour in contrast to higher excited states. Those are allowed to decay into a pair of D mesons ($c\overline{d}$, $\overline{c}d$) and are thus called 'broad states'. In the first initial hard parton collisions quark pairs ($c\overline{c}$) are created and the c quark and the $\overline{c}$ quark can combine to a J/ψ or with other produced quarks to D mesons. If a J/ψ has been formed, its decay products will be seen in the detectors. As described the J/ψ is a narrow state of the charmonium. It decays mainly into hadrons $(87.7 \pm 0.5)\,\%$, to $(e^+\ e^-)$ pairs $(5.94 \pm 0.06)\,\%$ and to $(\mu^+\ \mu^-)$ pairs $(5.93 \pm 0.06)\,\%$ [A$^+$08].
In case that a QGP is created, the high density of colour charges leads to a process analogous to Debye screening of electric charges that prevents the produced ($c\overline{c}$) pair from combining to a charmonium [SM86]. When the system freezes out (see figure 2.2 d) it is more likely that the c quarks will bind with other quarks and form D mesons because the light quarks are much more abundant. This suppression of the J/ψ compared with the collision of protons or light ions, where no QGP is created, has been observed at SPS [Gor00].
On the other hand, the number of charm-quark pairs is a function of the collision energy. At low energies the mean number of produced charm-quark pairs is fewer than one per collision, whereas at LHC energies it is about 200. That leads to the possibility that during hadronization c and $\overline{c}$ from different original pairs combine to form a J/ψ. This enhancement superimposes the suppression.
Analogous to the charm quark, the bottom quark (b) and its antiquark ($\overline{b}$) form a meson, which is called bottomonium. It has three narrow states Υ,Υ', Υ'', whose decays are suppressed, and broader states at higher energies. In contrast to the enhancement super-

imposing the suppression in case of J/ψ measurements, a clean suppression is expected for Υ measurements. This has not been observed at SPS and RHIC because there is much less Υ-yield than J/ψ-yield per collision. In addition the melting point ε of the Υ ($\varepsilon > 20$ GeV/fm^3) can only be reached at the LHC energies.
The only information available about the QGP are the particles, which are produced before the *thermal freeze out*, reaching the detector. At that time the QGP has already vanished and only its residues can be detected. The goal is to find the signals of the QGP in the measurements of those residues. Two possible signatures were mentioned above. The first one is the jet quenching and the second one is the J/ψ yield in comparison to the J/ψ yield in proton-proton collisions, where the energy densities are not high enough for the creation of the QGP. Furthermore, there is the possibility of observing strangeness enhancement, signatures of restoration of chiral symmetry and to analyse kinematic or electromagnetic probes (for details see [HM96]).

CHAPTER 3

Experimental Setup

The CERN where the LHC has been built was founded in 1954 and extends over the Franco-Swiss border near Geneva. Since then the nature of matter and the fundamental forces have been investigated there in several accelerator experiments.

3.1 The Large Hadron Collider

The Large Hadron Collider (LHC) is a gigantic scientific instrument and the largest machine ever built. The particle accelerator spans the border between France and Switzerland about 100 m underground in a tunnel of 27 km circumference (compare illustration 3.1). There are two beam pipes which accelerate protons or ions in opposite directions. Thereby the protons reach a velocity of 0.999999991 % of the speed of light c, this corresponds to a kinetic energy of the proton of 7 TeV. To achieve this 9539 superconducting magnets have been installed. These are mainly 1232 dipoles of 15 m length, 392 quadrupoles of 3 m length and 6000 corrector magnets. They operate in superfluid helium at 1.9 K [Ros03], [Gro08].
The two beams collide at four interaction points with a centre of mass energy of 14 TeV with a peak luminosity of $10^{34}\,\mathrm{cm}^{-2}\mathrm{s}^{-1}$ for proton-proton collisions and of 1150 TeV per collision of two lead ions with a luminosity of $10^{27}\,\mathrm{cm}^{-2}\mathrm{s}^{-1}$ [lhc95].
The collision energy at the LHC will be about 30 times higher than the energies reached at RHIC [Sch02]. The comparison of some system parameters like the final state multiplicity at *mid-rapidity*[1] can be seen in table 3.1. Due to the huge energy rise the experiments at the LHC will open a new physics domain that is expected with legitimate hope to lead to many new discoveries.

[1]The momentum is divided into its *longitudinal momentum* p_l and *transverse momentum* p_t. The *rapidity* is defined as $y = \frac{1}{2} ln(\frac{E+p_l}{E-p_l})$, in collider experiments $y = 0$ is called *mid-rapidity*

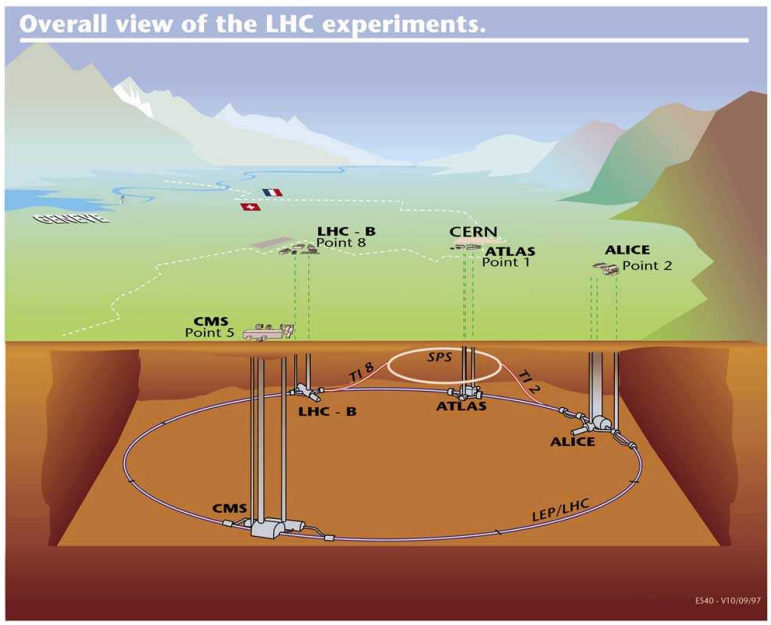

Figure 3.1: The Large Hadron Collider is located at the border district of France and Switzerland. [cer09]

	SPS	RHIC	LHC
$E_{cm}(GeV)$	17	200	5500
dN_{ch}/dy	500	700	$3000 - 8000$
$\varepsilon_{Bj}(GeV/fm^3)_{\tau_0=1fm/c}$	≈ 2.5	≈ 3.5	$15 - 40$
$V_{freeze}(fm^3)$	$\approx 10^3$	$\approx 9 \times 10^3$	$\approx 3.7 \times 10^4 - 1.0 \times 10^5$
$\tau_{QGP}(fm/c)$	< 1	≈ 1	$\approx 4.5 - 12$

Table 3.1: Comparison of system parameters at SPS, RHIC and LHC energies for heavy-ion collisions: The centre-of-mass energy E_{cm}, the multiplicity dN_{ch}/dy (values at *mid-rapidity*), the energy density ε_{Bj} after 'canonical' formation time τ_0, the freeze-out volume V_{freeze} and the QGP lifetime τ_{QGP}[Sch02].

There are six experiments located at the four interaction points, all run by international collaborations [Gro08].
ATLAS[2] and CMS[3] are designed to detect the myriad of particles produced in proton-proton collisions. They will analyse especially the nature of mass and are intended to prove the existence of the Higgs Boson. Furthermore, they search for particles predicted by supersymmetric extensions of the Standard Model. Because their detectors are designed independently from each other, confirmation of any new discoveries will be possible.

[2] A Toroidal LHC Aparatus
[3] Compact Muon Solenoid

The understanding of the imbalance of matter and antimatter in our universe is the motivation for LHCb[4]. It will measure CP violation in b-meson systems.
ALICE[5] is designed to analyse the QGP and its phase diagram. For more information see chapter 3.2. The two experiments TOTEM[6] and LHCf[7] are much smaller than the other experiments at the LHC and will study *forward particles*, which are protons and ions, which are only slightly deflected when the beams collide. TOTEM will provide information about the LHC collisions like total cross section and the luminosity. LHCf will use the forward particles as a source to simulate cosmic rays in laboratory conditions.

3.2 A Large Ion Collider Experiment

A Large Ion Collider Experiment (ALICE) is a dedicated heavy ion experiment, which will study strongly interacting matter in ultrarelativistic heavy ion collisions to explore the QCD phase diagram of nuclear matter. Therefore, it is designed to identify hadrons, leptons and photons and to offer the possibility of reconstructioning of short-lived particles like D mesons and their decay vertices.
It consists of two major parts, the central barrel which is embedded in the world's largest solenoid magnet with a field strength of 0.5 T in 1600 m^3 and the forward muon arm (see illustration 3.2) [atp08].

The central part covers polar angles at the interaction point from 45° to 135° over the full azimuth around the beam line. The beam pipe has a diameter of 1 mm and is surrounded by the Inner Tracking System (ITS), which consists of high resolution silicon tracking detectors. As particles carrying strange, charm, or bottom quantum numbers are-short lived, their decay vertices can be resolved by the ITS. The Time Projection Chamber (TPC) is a cylindrical barrel located outside the ITS. It is the major tracking system of ALICE recording the ionisation traces of traversing charged particles in about 560 000 channels. Due to the magnetic field of 0.5 T the trajectories measured by ITS and TPC are bent and therefore can be used to calculate the momentum of charged particles.
The following two detectors are designed for particle identification. The Transition Radiation Detector (TRD) which is able to distinguish between pions and electrons will be discussed in the following chapter. The enclosing Time Of Flight (TOF) detector measures the time it takes for each particle to travel from the interaction point to the surface of the detector with a resolution of 100 picoseconds.

[4]The Large Hadron Collider Beauty Experiment
[5]A LArge Ion Collider Experiment
[6]TOtal and Elastic Measurement
[7]Large Hadron Collider forward

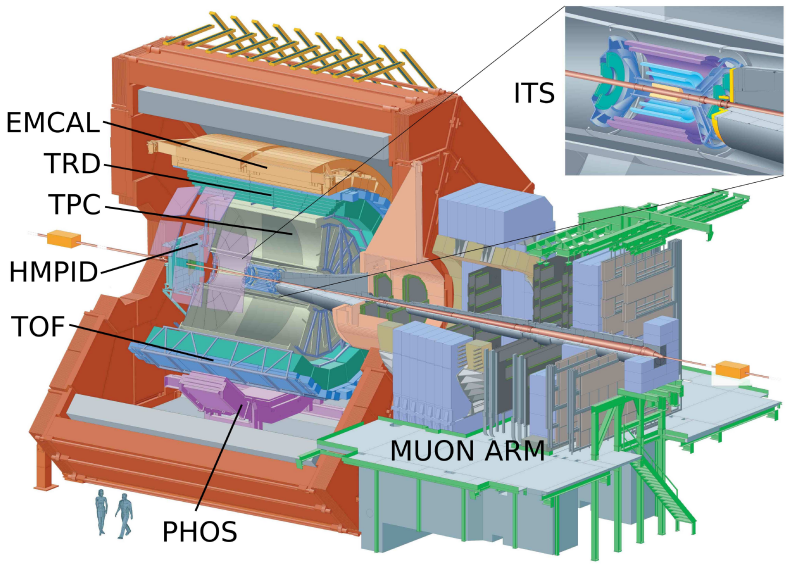

Figure 3.2: The ALICE Detector [Kle08]. It consists of the central barrel located in a solenoid magnet and the single arm forward muon spectrometer. The whole detector weights 10 000 tonnes and its material costs sum up to about 75 million Euro [Gro08].

Outside the TOF barrel some small area detectors are implemented. The Photon Spectrometer (PHOS) is an electromagnetic calorimeter whose crystals have densities comparable to lead but are as transparent as glass. It will measure photons and neutral mesons in a wide dynamic range with high energy and spatial resolutions. The Photon Multiplicity Detector (PMD) and the ElectroMagnetic CALorimeter EMCal will also measure photons but over a larger area with less precision. The measurement of photons provides information about the temperature of the system formed right after the collision. The High Momentum Particle Identification (HMPID) is a ring imaging Cherenkov detector and designed to identify high energy hadrons.

The forward muon arm is positioned at large *rapidities* at the forward direction of one beam line. Due to the fact that muons do not take part in strong interactions and do not emit bremsstrahlung at the quested energies they can pass a very thick and complex conical carbon absorber almost without being scattered. This effect is exploited to shield the muon detector from all other particles produced in the collision. It consists of ten tracking chambers, its own large dipole magnet, a second absorber wall made of iron and four trigger chambers. The complete spectrum of heavy quarkonia (J/Ψ,Ψ', Υ,Υ',Υ'') can be studied via their decays into $\mu^+\mu^-$ pairs.

3.3 Transition Radiation Detector

The Transition Radiation Detector (TRD) performs online tracking as well as particle identification. It consists of 540 Xe gas-filled pad ReadOut drift Chambers (ROCs), which are Multi Wire Proportional Chambers (MWPC), arranged in 18 SuperModules (SMs). Every SM contains 30 ROCs in five stacks and six layers. The resulting active area of roughly 700 m^2 is covered by almost 1.2 million readout channels. The SMs form a barrel of the size of 7.4 m in diameter and 7 m in length as it is shown in illustration 3.3. That translates into a *pseudorapidity*[8] coverage of $|\eta| < 0.9$ and an azimuthal coverage of 2π [tdr01]. The ALICE coordinate system has its point of origin at the nominal interaction point of the two beamlines. The x-axis is perpendicular to the local beam direction pointing to the accelerator centre. The y-axis is perpendicular to the x-axis and the mean local beam direction pointing upward and the z-axis is parallel to the mean local beam direction. The coordinate system of one ROC refers to the ALICE coordinate system for a SM positioned at $\Phi = 0\ ^\circ$ (see figure 3.3). In the following, all numbers will refer to the ROC coordinate system if not mentioned differently.

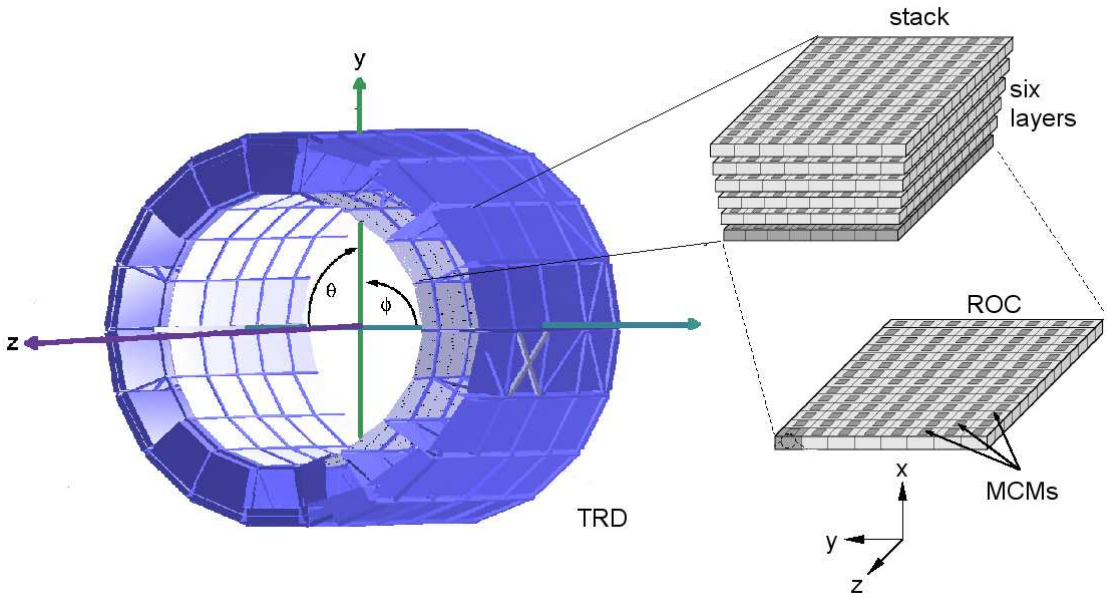

Figure 3.3: The 18 SMs form a barrel of the size of 7.4 m in diameter and 7 m in length. Each SM consists of 30 ROCs in six layers and five stacks. The coordinate system of one ROC (right) refers to the ALICE coordinate system (left) for a SM positioned at $\Phi = 0\ ^\circ$.

[8] Because it is complicated to measure the energy E, the *pseudorapidity* η has been defined for the case $E \ll m_0$: $\eta = \frac{1}{2}\ln(\frac{E+p_l}{E-p_l}) = -\ln \tan\frac{\Theta}{2}$

As explained in section 2.2 the behaviour of quarkonia like J/ψ and Υ in heavy ion collisions is a signature of the QGP. Due to their decay channel in electrons and positrons (e^+e^-) one possibility to study their production in the collision is to analyse the (e^+e^-) counting rates in the detectors. For this it is important that (e^+e^-) are distinguishable from charged hadrons like pions ($\pi^+\pi^-$). In 1999 the decision was made to add a TRD to the ALICE detector in order to increase the electron/pion seperation capability of ALICE by a factor of 100 for momenta above 2 GeV/c. In addition, the TRD can be used as an on-line trigger for high momentum electrons. That finally enables the whole detector to detect jets with energies above 100 GeV and to perform Υ measurements at mid-rapidity and J/ψ spectroscopy at large momenta. To distinguish between electrons and pions the TRD makes use of a relativistic quantum field effect called *Transition Radiation* (TR) (see section 3.3.2).

3.3.1 Design of the Read Out Chambers

The Design of the Read Out Chambers (TRD) consists of 540 ReadOut Chambers (ROCs) with each of them being a MWPC detector. These are devided into a radiator, a drift region and an amplification region. In addition, on top of the ROC front-end electronics are installed which are discribed in chapter 3.3.4. An overwiew of the setup is given in figure 3.4.

The radiator forms the bottom of the chamber and is 4.5 cm high. It consists of polypropylene fibre mats, which are embedded in Rohacell foam sheets. If an ultrarelativistic particle with a velocity v resulting in the so-called Lorentz factor[9] γ of the particle being ≥ 1000 crosses these materials of extreme inhomogeneous optical density, a relativistic quantum field effect leads to the emission of so-called Transition Radiation (TR). The TR was predicted by Ginzburg and Frank in 1945 [GF45] and is produced when a charged particle moves through a surface between two media of different dielectric constants. In case of ultrarelativistic particles TR photons are created having wavelengths similar to those of x-rays with a probability that is linearly dependent on the Lorentz factor γ of the particle. The angular distribution of the TR is peaked forward and has a sharp maximum at $\delta = \frac{1}{\gamma}$.

After passing the radiator the particle and eventually produced TR enter the drift region of the chamber (see illustration 3.4). It is 3.0 cm high and filled with a Xe/CO_2 gas mixture at LHC to be able to measure transition radiation to separate electrons from the pion background. In Münster an Ar/CO_2 mixture is used because it is far less expensive and mainly muons from cosmic rays are measured (see chapter 4) that do not produce TR. The bottom of the drift region is the drift electrode (with U_D = -2000 V) and on the opposite end it is terminated by a plane of cathode wires which are on ground potential

[9] Lorentz factor of a particle: $\gamma = \frac{1}{\sqrt{1-\beta^2}}$, $\frac{v}{c} = \beta$

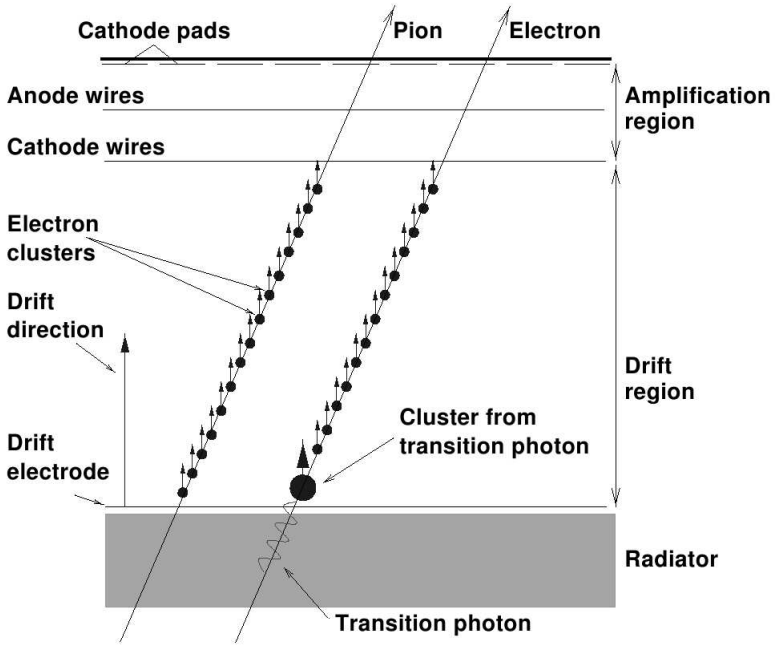

Figure 3.4: Cross section through a TRD detector module (ROC) [GO05]. The primary particle ionises gas atoms in the drift and amplification region. The generated electrons drift to the anode wires, where by gas amplification in the range of 10^4 a measurable signal on the cathode pad plane is created.

(see illustration 3.4). The gaps between the cathode wires are 2.5 mm wide. In the drift region free electrons are created through ionisation by traversing high energy particles and TR photons. The generated electrons drift towards the cathode wires and enter the amplification region at a certain time after the ionisation. The drift velocity of the electrons is constant and much smaller than the velocity of the primary particle. Thus the period of time from ionisation until the electron reaches the cathode wires is a function of the distance in x-direction of the point of ionisation and the cathode wire plane. The amplification region is 0.7 cm high and ends at the cathode plane (ground potential). The cathode plane spans in the y, z-plane and is divided in 16 and twelve 'rows' respectively in z-direction and in 144 'columns' in y-direction. All resulting 'pads' are slightly tilted with respect to the z-axis. The design of the cathode pad plane is illustrated in figure 3.5.

There are twelve different pad geometries, with six of them having a different inner pad width W. That is due to the fact that the ROCs of different layers cover areas of different size. Corresponding to the six layers in one SM there are six different 'ROC-types' with respect to the inner pad width. There are two different versions of every ROC-type that differ in their number of pad rows. The ROCs which will be installed in stack two in the SM (C0) have only twelve rows and thus are smaller than the ROCs in the other stacks (C1) that have 16 rows. The pad geometry of all different ROCs are given in table 3.2.

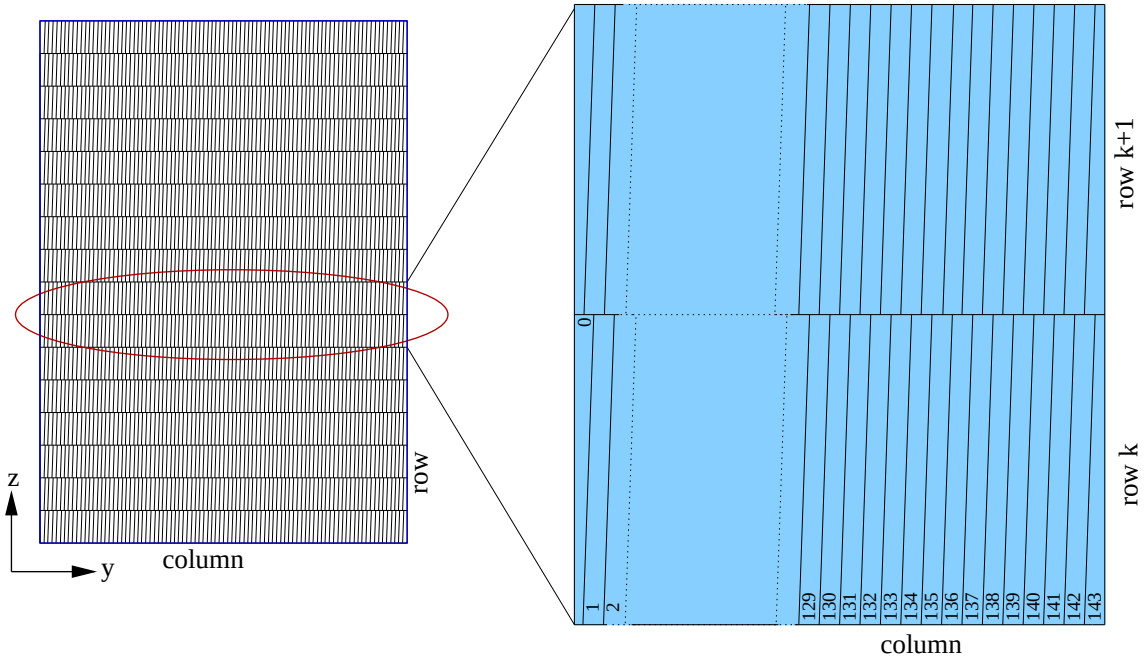

Figure 3.5: The pad plane is located in the y, z-plane. It is subdivided in rows and columns. The pad sizes can be found in table 3.2.

The anode wire plane ($U_A = 1400\,\mathrm{V}$) is located centrally between the cathode wire plane and the pad plane. The width of the gaps between the wires is 5 mm.
In the amplification region the electrons liberated by the primary particle in ionisation processes are accelerated towards the anode wires. They gain energy and start to ionise more and more gas atoms near the anode wires, leading to gas amplification in the range of 10^4 by avalanche creation.

type	♯ rows	α_{tilt} (°)	L_{rim}	W_{rim}	L_{opad}	L_{ipad}	W_{opad}	W_{ipad}
L0C0	12	-2	10	5	80.0	90.0	5.15	6.35
L0C1	16	-2	10	5	75.0	75.0	5.15	6.35
L1C0	12	+2	10	5	80.0	90.0	5.85	6.65
L1C1	16	+2	10	5	75.0	75.0	5.85	6.65
L2C0	12	-2	10	5	80.0	90.0	7.05	6.95
L2C1	16	-2	10	5	75.0	80.0	7.05	6.95
L3C0	12	+2	10	5	80.0	90.0	7.75	7.25
L3C1	16	+2	10	5	75.0	85.0	7.75	7.25
L4C0	12	-2	10	5	80.0	90.0	8.45	7.55
L4C1	16	-2	10	5	75.0	90.0	8.45	7.55
L5C0	12	+2	10	5	80.0	90.0	9.65	7.85
L5C1	16	+2	10	5	85.0	90.0	9.65	7.85

Table 3.2: The dimensions of the TRD pad planes for all individual chamber types. The sizes are in mm. ♯ rows are the number of rows in z-direction in one chamber. L_{rim} and W_{rim} are the size of the rim in z-direction and in y-direction. L_{opad}, L_{ipad} and W_{opad}, W_{ipad} are the length and the width of the pads. The size of the pads in the two outer rows of the pad plane (*opad*) usually differs from the size of the pads of the inner rows (*ipad*). [Ems05].

3.3.2 Electron Identification

The production rate of the quarkonia J/ψ and Υ is one signature of the QGP. Both have a decay channel in (e^+e^-) and thus, the electron identification is the main goal of the TRD. Due to their larger $(\beta \cdot \gamma)$ electrons deposit more energy in the drift chamber than charged pions with the same momentum, as a consequence of the Bethe-Bloch equation [A+08]. Thus the average deposited charge q_{mean} is a classical possibility to seperate electrons from pions.
The design of the ROCs provides an additional possibility of electron identification exerting the relativistic quantum field effect of TR. Due to their much larger Lorentz factor γ, electrons produce TR while crossing the radiator in contrast to pions and other hadrons. The produced TR photons are predominantly absorbed at the beginning of the drift region, after leaving the radiator. The conversions of the TR photons are superimposed on the usual ionisation energy loss of the primary particle. Due to the constant drift velocity of the generated electrons in the drift region the TR leads to an increase of the recorded signal at higher drift times. Thus the sampled signals originating from electrons show a different temporal behaviour than the signal originating from pions.
If the drift time information is employed in a so-called bidimensional likelihood, for which the total deposited charge is used together with the distribution of the time bins with the maximum measured amplitude, the pion rejection capability can be improved by about 60 % compared with the standard likelihood method on total deposited charge [A+04]. Furthermore, the electron/pion seperation can be improved if a neural network algorithm[10] is exerted, which analyses the temporal behaviour of the signal by exploiting the signal information from every single time bin.

3.3.3 Creation of the Signal on the Pad Plane

In the amplification region of the ROCs electrons and ions are generated in the created avalanches. The electrons move to the nearest wire of the anode wire plane and reach the surface of the wire in less than one nanosecond, whereas the created ions move away from the wires with a velocity that is thousand times smaller than the velocity of the electrons. A charge in the amplification region induces a signal on the cathode plane. For the purpose of coordinate measurements the cathode plane is subdivided into several parts and thus called pad plane. Due to the fact that each pad has a rather high capacity of about $C_{\mathrm{pad-ground}} \approx 6\,\mathrm{pF}$, the fast electrons do not provoke a measurable signal in contrast to the slower ions.

[10] The neural network algorithm and its electron/pion sepeartion performance will be studied in [Wil09].

Pad Response Function

If a charge q is placed in the amplification region at the distance x_0 in front of the pad plane, it induces a charge on the metal surface. The resulting surface charge density is given by $\sigma(y,z) = \varepsilon_0 E_x(y,z)$. $E_x(y,z)$ is the electric field on the metal surface and can be calculated by assuming an 'image charge' -q behind the surface at -x_0 [BRR08]

$$E_x(y,z) = -\frac{qx_0}{2\pi\varepsilon_0(x_0^2+y^2+z^2)^{\frac{2}{3}}}; \qquad E_z = E_y = 0. \tag{3.1}$$

The integral of the charge density over the metal surface is the total charge Q induced on the plane

$$Q = \int_{-\infty}^{\infty}\int_{-\infty}^{\infty}\sigma(y,z)dydz = -q. \tag{3.2}$$

The total charge induced on the whole plane is independent of the distance x_0. By integrating $\sigma(y,z)$ over the area of each pad the induced charge on every single pad can be determined. The pads are rectangles with the long side L in z-direction perpendicular to the wires of the anode wire plane. Since this side is large compared with the diameter of the area mainly affected by the charge q of the avalanche, the integration of $\sigma(y,z)$ over z can run from -∞ to ∞. The short side W is much smaller so that the avalanche is expected to induce charge on about three adjacent pads in y-direction. This 'charge sharing' enables the position of the avalanche to be reconstructed with a resolution higher than the pad width W.
The induced charge e.g. on the central hit pad, which means the pad nearest to the avalanche, is given by:

$$Q_1(x_0) = \int_{-\infty}^{\infty}\int_{-\frac{W}{2}}^{\frac{W}{2}}\sigma(y,z)dydz = -\frac{2q}{\pi}\arctan(\frac{W}{2x_0}). \tag{3.3}$$

Since the charge induced on a single pad depends on the distance x_0 to the pad plane, the movement perpendicular to the pad plane of the charge q with a velocity v leads to a change of the charge induced on the single pad and thus to the induced current

$$I_1^{ind}(t) = -\frac{d}{dt}Q_1([x_0(t)]) = -\frac{\partial Q_1([x_0(t)])}{\partial x_0}\frac{dx_0(t)}{dt} = \frac{4qW}{\pi[4x_0(t)^2+W^2]}v. \tag{3.4}$$

To be able to reconstruct the position of the charge q in the anode wire plane using the signals induced on the single pads of the pad plane, the so-called *Pad Response Function* (PRF) is applied. It determines the fraction of the total signal being induced on one single pad of the pad plane as a function of the distance between the centre of the pad and the charge q. Thereby, the distance is measured as a projection onto the pad plane.
To determine the PRF Gatti et al. [G$^+$79] and Mathieson et al. [MG84] use the cathode

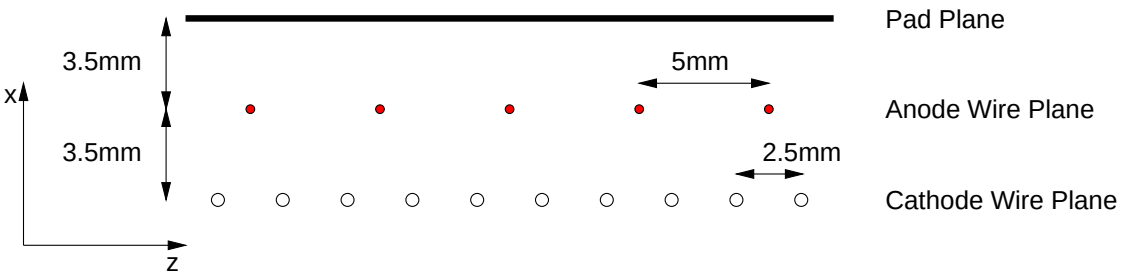

Figure 3.6: The two cathode planes (cathode wire plane and pad plane) and the centrally between them positioned anode wire plane in the ROC [tdr01].

charge distribution $\Gamma(\lambda)$. It provides the signal on a pad of infinitesimal width and is thus defined by

$$dI_{c1}(t,\lambda) = I_c(t)\Gamma(\lambda)d\lambda; \qquad \int_{-\infty}^{\infty}\Gamma(\lambda)d\lambda = \frac{1}{2}, \tag{3.5}$$

where $I_c(t)$ is the induced signal on the whole cathode. $I_{c1}(t)$ is the signal induced on one of the two cathode planes. $\lambda = \frac{y}{h}$ is the distance of that infinitesimal pad to the position of the avalanche. This distance is projected onto the pad plane and given in units of the distance from the pad plane to the anode wire plane $h = 3.5$ mm (see illustration 3.6).
The charge in the anode wire plane induces a signal on both cathode electrodes. These are the cathode wire plane and the pad plane (see illustration 3.6). Since $\Gamma(\lambda)$ is integrated over the pad plane only in equation 3.5, the result is $\frac{1}{2}$ of the total signal induced on both cathode planes.

For $\Gamma(\lambda)$ [G$^+$79] and [MG84] give an empirical formula, which is a single parameter expression:

$$\Gamma(\lambda) = K_1\frac{1-\tanh^2 K_2\lambda}{1+K_3\tanh^2 K_2\lambda}. \tag{3.6}$$

K_1 und K_2 are uniquely defined by K_3

$$K_1 = \frac{K_2\sqrt{K_3}}{4\text{atan}\sqrt{K_3}} \qquad K_2 = \frac{\pi}{2}(1-\frac{\sqrt{K_3}}{2}). \tag{3.7}$$

K_3 is a function of the chamber geometrical parameters h, the radius a and the gap s of the anode wires.
Equation 3.6 gives the cathode charge distribution. To get the fraction of charge induced on a single pad at position λ, $\Gamma(\lambda)$ has to be integrated over the pad width W

$$
\begin{aligned}
I(t,\lambda,W) &= \int_{\lambda-W/2}^{\lambda+W/2} dI_{c1}(t,\lambda')d\lambda' = I_c(t)\int_{\lambda-W/2}^{\lambda+W/2}\Gamma(\lambda')d\lambda' \qquad (3.8)\\
&= I_c(t)\frac{K_1}{K_2\sqrt{K_3}}(\arctan[\sqrt{K_3}\tanh K_2(\lambda+\frac{W}{2})] - \arctan[\sqrt{K_3}\tanh K_2(\lambda-\frac{W}{2})])\\
&= I_c(t)P_0(\lambda)
\end{aligned}
$$

where $P_0(\lambda)$ is the sought-after Pad Response Function.

Improvement of the z-resolution

Whereas the width W of the pads is chosen in a way that charge sharing between several adjacent pads is achieved, the length of the pads is much bigger than the expected diameter of the area on the pad plane effected by the avalanche. Hence the position resolution in z-direction would be restricted to the length of the pads:

$$z_{row} - \frac{L}{2} < z < z_{row} + \frac{L}{2}, \qquad (3.9)$$

z_{row} being the z-coordinate of the centre of a pad row [tdr01]. To improve the z-resolution the pads have been tilted 2 ° with respect to the z-axis (see illustration 3.5). The tilt is performed alternating +2 ° and -2 ° in consecutive layers. Due to the tilt the measurements of the position in y-direction and z-direction are no longer independent. That leads to a systematic error in the reconstruction of the y-position using the information obtained by one ROC. But if the information of several ROCs that the particle has crossed is employed in a tracking algorithm to reconstruct the particle track, the z-resolution can significantly be improved compared with the z-resolution given in equation 3.9 without significant decline of the y-resolution.

Time Response Function

To determine the total time response of the detector three effects have to be taken into account. The first one is the rather slow drift velocity of the ions, which are created in the avalanche. They induce a signal on the pads with a long tail of several microseconds duration called the ion tail. The second effect is the non-isochronity of the electron drift. The resulting drift time of the ionisation electrons depends on the distance of the electron to the nearest anode wire in z-direction when it enters the amplification region. In addition to these two effects that are determined by the ROC design, the time response function is influenced by the response of the preamplifier/shaper (see chapter 3.3.4) to an incoming signal. Figure 3.7 shows the time response function of a signal corresponding to a 6 keV point charge deposit, generated with a GARFIELD simulation [Bia99].

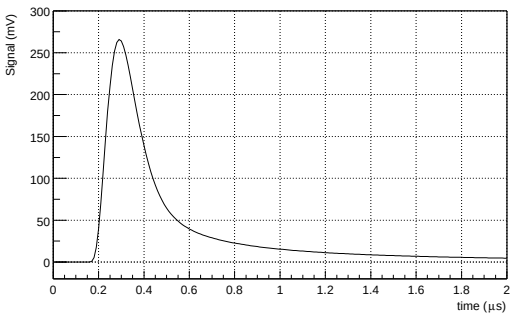

Figure 3.7: The time respone function of the preamplifier/shaper to a pad signal simulated with GARFIELD for a 6 keV point charge deposit [tdr01].

3.3.4 Data Readout by Front-End Electronics

The main part of the Front-End Electronics (FEE) of the TRD is located directly on the ROC. Thus data processing as well as compression is possible at a very early stage in the readout chain.

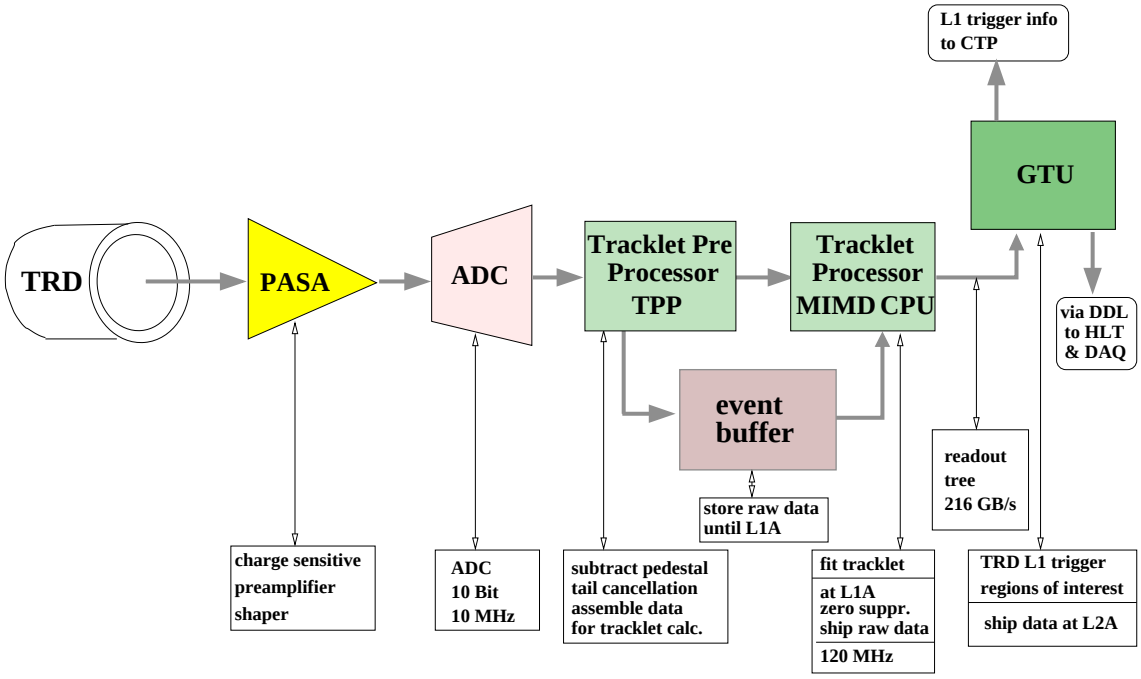

Figure 3.8: The readout chain of the TRD [tdr01].

The basic logical components of the FEE are illustrated in figure 3.8. The signals of the pads are amplified in a charge sensitive PreAmplifier/ShAper (PASA) and afterwards digitized in a 10 Bit/10 MHz low power ADC. It is followed by a digital circuitry which performs online tracking and storage of the raw data for subsequent readout. It consists of a digital filter, the Tracklet PreProcessor (TPP), the event buffer and the Tracklet

Processor (TP). The TP is a micro CPU implemented as Multiple Instruction Multiple Data (MIMD) processor. It ships the data via the readout tree to the Global Tracking Unit (GTU). Every component of the readout chain but the GTU is located directly on the ROC. The external GTU merges the information of the ROCs to particle tracks through a whole SM. The track information is sent to the Central Trigger Processor (CTP) of ALICE. It is used to issue a trigger decision.
The PASA is connected to 18 pads of the cathode pad plane, which are adjacent in y-direction. It amplifies the charge fluctuations on its input ports by a factor of 10 $\frac{\text{mV}}{\text{fC}}$. The so-called TRAP chip ('TRAcklet Processing') contains the ADCs, the TPP, the event buffer and the TP. It receives the analogue signals of the 18 differential voltage output ports of the PASA and in addition the signal of three pads of adjacent PASAs. The PASA and the TRAP chip are combined to a Multi Chip Module (MCM).

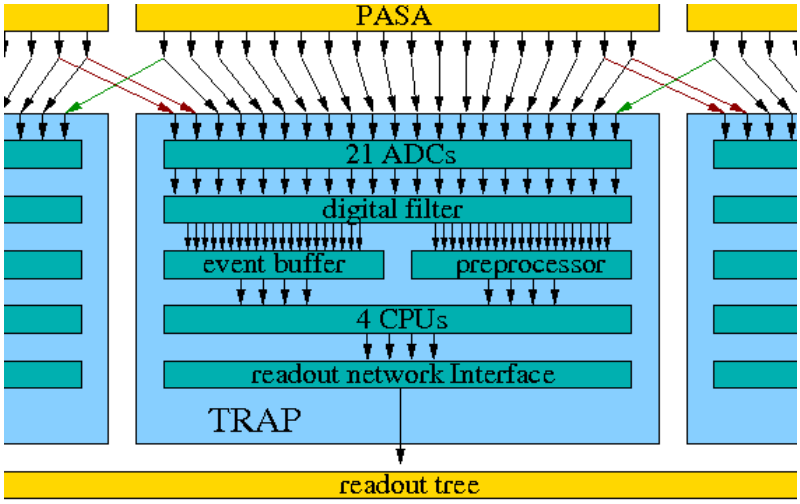

Figure 3.9: The main signal path in the TRAP chip based on M. Gutfleisch [Gut06].

Illustration 3.9 shows the main path of the signal in the TRAP chip. The differential analogue output signal of the PASA is cyclic successively approximated in the ADCs with a sampling rate of 10.0 MHz. Thus the duration of a readout time bin is 0.1 μs. The digital output signal is received by the digital filter, where several corrections are applied and the signal is distributed to the event buffer and the TPP.

The Digital Filter

The digital filter consists of five stages. The nonlinearity correction remedies nonlinear effects, which appear in the amplification and digitalisation. Therefore, it uses a common correction Look-Up Table (LUT). The second stage is the pedestal correction. This is a

recursive filter of first order and it provides a well-defined baseline value of the signal that is usually 10 ADC channels. It is necessary because otherwise the output signal of the PASA is changing in time and shows variations in different channels. The next step is the gain correction filter. It is calibrated based on offline analysis of the amplitude spectrum and corrects the influence of local fluctuations in the gas amplification, the amplification of the PASA and the conversion gain of the ADCs. These three effects are due to small differences in the chip fabrication and chamber geometry.
In chapter 3.3.3 the creation of so called ion tails is described. Drifting to the pad plane with a rather low velocity, the ions induce a signal on the pads which shows a temporal behaviour. It rises within nanoseconds and has a tail, which extends for microseconds. The tail can be sufficiently approximated by a two exponential approach and thus the temporal behaviour of the gas amplification is given by the impulse response $S(t)$:

$$S(t) = 1_{(t\geq 0)} \sum_{n=1}^{N} \alpha_n e^{\kappa_n t} + R_{N(t)} \tag{3.10}$$

with $N = 2$. The time t is measured in terms of time bins and $R_{N(t)}$ can be neglected in the following. The first exponetial function used describes the fast decay ($\alpha_S, \lambda_S = e^{-\kappa_S}$) and the second one escribes the slow decay ($\alpha_L, \lambda_L = e^{-\kappa_L}$) of the signal. Because the order of magnitude of the two decay constants λ_L and λ_S is known [Gut02], the dynamic range in which they can be chosen with a granularity of 2^{-11} can be limited. The hardware implementation of the tail calculation is given by

$$\begin{aligned} S(t) &= 1_{(t\geq 0)}[\alpha_L \lambda_L^t + (1-\alpha_L)\lambda_S^t], \\ \alpha_S &= (1-\alpha_L), \\ \alpha_L &= [0, 0.5), \\ \lambda_L &\in [0.75, 1), \\ \lambda_S &\in [0.25, 0.5). \end{aligned} \tag{3.11}$$

Using this formula the tail cancellation filter subtracts the tail caused by the previous time bins from the input value given by the gain correction filter.
The last step in digital filtering is the crosstalk suppression. It is a two-dimensional filter matrix which suppresses the capacitive coupling of neighbouring pads including their connectivity to the PASA chip. The disturbances in the direct neighbour pads would otherwise reach amplitudes in the percent range with respect to the peak amplitude. The calibration process for its entries as well as for the other four parts of the digital filter is described in [Gut06].

Zero Suppression in the Event Buffer

The event buffer stores the raw data of the events for the subsequent raw data readout. It consists of 21 independent memory blocks 64 × 11 bits each. Its write port is operated at 10 MHz as this is the sampling rate of the ADCs which are continuously active. In contrast to that, the readout is event oriented and thus the read ports are operated at the frequency of the four CPUs (120 MHz). The CPUs read out the event buffer with a unique assignment of each CPU to the 21 channels of the event buffer. In the event buffer the selection of the channels is made, which are supposed to carry a part of a signal created by passing particles. Therefore, a set of indicator bits is used, which are transmitted to one of the CPUs in the TP where the 'channel transmission mask' is created. If a pad fulfils the required condition in one time bin, the recorded signal of all time bins of the event are shipped to the readout tree. The indicators are a configurable combination of 3 possible citeria, for which it is important to notice that parts of the TRAP follow an 'inverse logic':

The first criterium is that the signal on pad i is a 'local maximum'. The pad i will be read out in all time bins (tb) of the event if it is a local maximum in at least one time bin.

$$I_{0,i}(tb) = \begin{cases} 0 & \text{, if} \quad Q_i(tb) \geq Q_{i-1}(tb) \quad \text{and} \quad Q_i(tb) \geq Q_{i+1}(tb) \\ 1 & \text{, otherwise} \end{cases} \tag{3.12}$$

The second criterium: The pad is read out if the sum over the charge of this pad and its two neighbours reaches a certain cluster threshold T_{IT}.

$$I_{0,i}(tb) = \begin{cases} 0 & \text{, if} \quad Q_i(tb) + Q_{i-1}(tb) + Q_{i+1}(tb) = Q_{i,sum} \geq T_{IT} \\ 1 & \text{, otherwise} \end{cases} \tag{3.13}$$

The third criterium: The pad is read out if its signal amplitude reaches a certain single threshold T_{IS}.

$$I_{0,i}(tb) = \begin{cases} 0 & \text{, if} \quad Q_i(tb) \geq T_{IS} \\ 1 & \text{, otherwise} \end{cases} \tag{3.14}$$

Every logical combination of these three criteria can be chosen as requirement that a certain pad is marked to be read out. In addition, the two neighbouring pads of a pad which fulfils the requirement can always be read out as well (*neighbour flag* = 0).
This data compression by reading out only certain pads in one event is called zero suppression. The calibration process for the thresholds T_{IT} and T_{IS} is described in chapter 8.

The Tracklet Preprocessor and the Tracklet Processor

The task of the TPP and the TP is to parameterise particle tracks and calculate tracklets. A tracklet is a linear fit of that segment of the particle track which passes through one ROC. For the calculation the position information gained from so-called hits in consecutive time bins is used. A hit is a signal distribution caused by a passing particle on adjacent pads in one time bin. The structure of the TPP is illustrated in figure 3.10.

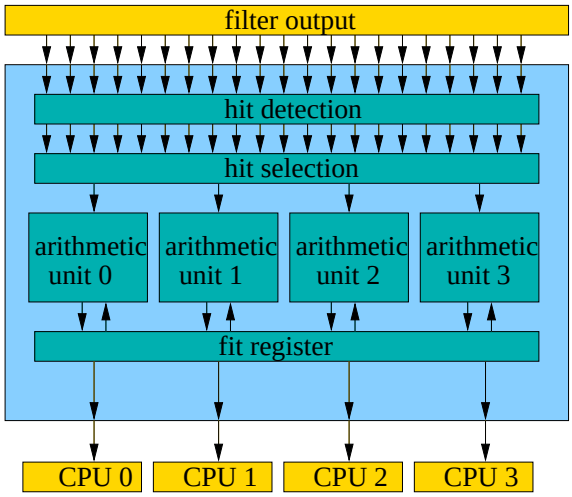

Figure 3.10: The tracklet preprocessor consists of the hit detection unit, the hit selection unit, four arithmetic units and the fit register file. Based on M. Gutfleisch [Gut06].

The hit detection unit processes the 21 output channels of the digital filter. It depends on two conditions if a channel i is marked to be the centre of a hit. First, the induced charge on the pad has to be a local maximum

$$Q_i(tb) \geq Q_{i-1}(tb) \quad \text{and} \quad Q_i(tb) \geq Q_{i+1}(tb). \tag{3.15}$$

Second, the total charge Q_{sum} of the three pads involved in the possible hit reaches a certain threshold

$$Q_{sum} = Q_i(tb) + Q_{i-1}(tb) + Q_{i+1}(tb) \geq T_{Hit} \ . \tag{3.16}$$

If more than four pads have been recognised to be a centre of a hit, the hit selection unit determines the four hits with the largest Q_{sum} and forwards the hit information of each of them to one of the arithmetic units. The hit information consists of the pad number i, the total charge Q_{sum} and the filtered charge of the three pads $Q_i(tb)$, $Q_{i-1}(tb)$, $Q_{i+1}(tb)$. For the following calculations the baseline is substracted from all charge values.
Since the TRD is designated to perform high energy electron tracking, the track segments in one ROC can be approximated by a straight line model ($y = \vartheta x + \widehat{y}$). Here (x, y) is the

reconstructed position of the ionisation process in the drift region of the ROC in one time bin. Whereas x is given by the number of the tb, y has to be calculated using the charge distribution on the pads of the pad plane. The explanation of the calculation of y in the TPP is given in chapter 7.
As the ADCs are sampling at a frequency of 10 MHz, the TPP calculates the tuple (x, y) every 0.1 μs and from that on it updates the following fit sums in the fit register file with the same frequency

$$\begin{aligned} X &= \sum_{n=1}^{N} x_n, \qquad Y = \sum_{n=1}^{N} y_n, \qquad XY = \sum_{n=1}^{N} x_n y_n \\ X^2 &= \sum_{n=1}^{N} x_n^2, \qquad Y^2 = \sum_{n=1}^{N} y_n^2, \qquad N = \sum_{n=1}^{N} N, \\ Q^0 &= \sum_{n=k(0)}^{N-m(0)} \frac{1}{4} \cdot Q_{sum}, \qquad Q^1 = \sum_{n=k(1)}^{N-m(1)} \frac{1}{4} \cdot Q_{sum}. \end{aligned} \tag{3.17}$$

Here N is the number of hits of the addressed channel. After the readout time the four CPUs, which constitute the TP, read out the fit sums from the fit register file. As the slope is expected to be rather small, the two parameters of the fit, ϑ and $\widehat{y}$, are approximately given by

$$\vartheta = \frac{N \cdot XY - XY}{NX^2 - XY}, \tag{3.18}$$

$$\widehat{y} = \frac{N^2 Y - X \cdot XY}{NX^2 - XY} \ . \tag{3.19}$$

The fit error can be estimated to be

$$\sigma_y^2 \chi^2 = NY^2 - YY - \frac{(N \cdot XY - XY)^2}{NX^2 - XX} \ . \tag{3.20}$$

After the readout is finished the hit information including the channel number i, the number of hits of the addressed channel N, Q_{sum} and the fit sums (see equations 3.17) of up to four hits per time bin is stored in the fit register file. Because tracks are expected to be rather stiff, the hit information dedicated to one tracklet is in good approximation stored on two adjacent pads. The fit register file possesses a specialised hardware to choose the four pairs of adjacent pads, for which the hit information is assigned to one of the four CPUs of the TP for further calculations.

First the pad pairs are analysed if they meet the condition

$$N_i \geq T_{N_{\text{Left}}} \quad \text{and} \quad N_i + N_{i+1} \geq T_{N_{\text{total}}},$$

where $T_{N_{\text{Left}}}$ and $T_{N_{\text{total}}}$ are the thresholds for the minimum number of hits in the left channel and in both channels respectively. If $T_{N_{\text{Left}}}$ is set to 1, at least the left channel is involved in the tracklet. $T_{N_{\text{total}}}$ is typically chosen such that the concerning channel pair has hits in more than 40 % of the samples in both channels. Afterwards the four pairs with the maximum number of hits are marked to be tracklet candidates and assigned to the four CPUs.
In the CPUs the fit sums of the channel pairs are merged. The coordinates of the right channel are transformed to coordinates relative to the centre of the left channel.

$$(x, y)_{i+1} \rightarrow (x, y + W)$$

Afterwards the parameters of the fit, which are the slope ϑ and the offset $\widehat{y}$, are calculated based on the merged fit sums according to the equations 3.18. In addition, the probability that a tracklet has been caused by an electron P_{electron} is calculated using Q^0 and Q^1 (see equations 3.18). A classical criterion to seperate electrons from the pion background is the mean charge per ionisation process q_{mean}

$$P_{\text{electron}} = P_{\text{electron}}(\frac{Q_{\text{total}}}{N}) = P_{\text{electron}}(q_{\text{mean}}).$$

Exploiting the effect of TR, the temporal behaviour of the signal can be used for electron identification. It is analysed by the comparison of the two partial charge accumulations along the tracklet Q^0 and Q^1. The obtained information will be given in eleven bits, which choose an eight bit LUT entry that gives the electron probability of the tracklet. The entries of the LUT just like the ideal range of the charge accumulations are still under investigation.
In the final step the parameters ϑ and $\widehat{y}$ are transformed to the GTU coordinate system ($\tilde{\vartheta}$,$\tilde{\widehat{y}}$) and ϑ is scaled to the deflection length. This is the difference of the y-coordinates between the start of the tracklet and the end of the tracklet. Afterwards ($\tilde{\vartheta}$,$\tilde{\widehat{y}}$) are combined with the information about the pad row and the electron probability $P_{electron}$ to a 32 bit word (see table 3.3), which is shipped to the readout tree. For a more detailed description of the electronic sequences see [Gut06].

parameter	**symbol**	**granularity**	**range**	**bits**
pad position	$\tilde{\hat{y}}$	160 μm	[-643.2 mm, 643.2 mm]	13
deflection length	$\tilde{\vartheta}$	140 μm	[-8.8 mm, 8.8 mm]	7
pad row		1	[0,15]	4
electron probability	$P_{electron}$	0.39 %	[0,1]	8

Table 3.3: Bin content of a tracklet word [dC03].

CHAPTER 4

Supermodule Test Setup

Since cosmic rays are an abundant source of high energetic charged particles, they provide a good possibility for calibration of the SMs assembled at Münster. In the absence of a magnetic field, this high-energy radiation leads to linear tracks through the whole SM.

4.1 Cosmic Rays

'Primary' cosmic rays are products of nucleosynthesis and electrons accelerated at astrophysical sources, while 'secondary' cosmic rays are produced in interactions of the primaries with interstellar gas. Thus, they are no end products of nucleosynthesis in contrast to the primaries [Y+06]. Traversing the universe, cosmic rays including all stable charged particles and nuclei with a lifetime of at least 10^6 years hit the atmosphere of the earth. Those which pass the sun are decelerated by solar winds, which leads to a measurable anticorrelation between solar activity and the intensity of cosmic rays at energies below 10 GeV. Free protons represent 79 % of the nucleons in the primary cosmic rays, while about 15 % of the nucleons are bound in helium. In interactions of cosmic rays in the atmosphere myriads of particles are produced which are called 'cosmic showers' (see illustration 4.1).

The protons from cosmic rays interact with nuclei in the atmosphere like oxygen or nitrogen at a height of 15 - 20 km. Thereby mainly pions and less kaons are produced in a ratio of 10:1. Charged mesons decay into muons and neutrinos, whereas neutral mesons decay into electrons, positrons and photons (see illustration 4.1). Some mesons interact with other particles before they decay due to their finite lifetime. The mean lifetime of pions is 26 ns and that of kaons is 12.4 ns. Approximate analytic solutions of the set of coupled cascade equations, which describe the flux of cosmic rays through the atmosphere, lead to a vertical intensity of nucleons at the depth X of [Y+06]

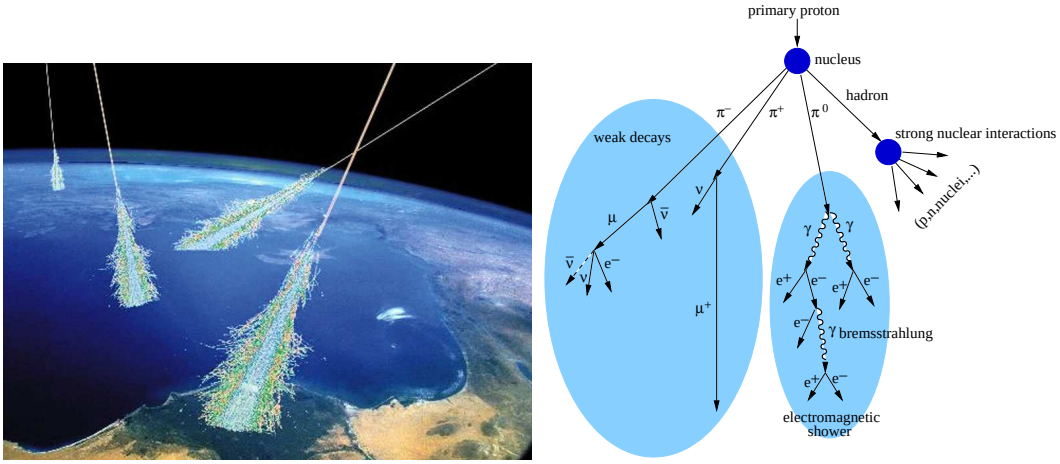

Figure 4.1: Cosmic rays hit the atmosphere of the earth. By interaction with the nuclei in the air (e.g. N and O) cosmical showers are produced (left panel: [Swo] , right panel [KB04]).

$$I_N(E, X) \approx I_N(E, 0)e^{-X/\Lambda}. \tag{4.1}$$

Here Λ is the attenuation length of nucleons in air. With $Z_{N\pi}$ being the spectrum-weighted moment of the inclusive distribution of charged pions in interactions of nucleons with nuclei in the atmosphere, the intensity of charged pions for an energy $E_\pi \ll \epsilon_\pi = 115\,\mathrm{GeV}$ is given by [Y+06]

$$I_\pi(E_\pi, X) \approx \frac{Z_{N\pi}}{\lambda_N} I_N(E_\pi, 0)e^{-X/\Lambda} \frac{X E_\pi}{\epsilon_\pi}.. \tag{4.2}$$

Most important for the SM test setup are the particle and energy distributions of the cosmic rays at sea-level. Muons are the most numerous charged particles hitting the SM. Their mean energy is approximately 4 GeV and their integral vertical intensity is $70\,\mathrm{m^{-2}s^{-1}sr^{-1}}$. The overall angular distribution is $\propto \cos^2 \Theta$. That fits well with muons of 3 GeV, whereas the angular distribution becomes steeper at lower energies and flattens at higher energies. Electrons, positrons and photons constitute the electromagnetic component of the cosmic rays at sea-level. They originate from muon decay and the decay of neutral pions. Their integral vertical intensity is $\approx 0.2\,\mathrm{m^{-2}s^{-1}sr^{-1}}$ for energies higher than 1 GeV, where the ratio between photons and the sum of electrons and positrons is ≈ 1.3.
Some of the nucleons of the primary cosmic radiation reach sea-level and additional nucleons are produced in strong nuclear interactions. At sea-level one third of them are neutrons. The vertical intensity is given by equation 4.1. For protons above 1 GeV it is $\approx 0.9\,\mathrm{m^{-2}s^{-1}sr^{-1}}$.

4.2 Cosmic Trigger

The purpose of the trigger is to provide a trigger-signal when a particle passes the detector. Because the expected particles originate from cosmic rays the trigger is called ‘cosmic trigger‘. If the detector, in this case all 30 ROCs in the SM, has received a trigger-signal, all channels are read out. The readout chain is described in chapter 3.3.4.
The cosmic trigger is a combination of a detector and a logic circuit. The detector part consists of two layers of organic scintillators linked with photomultipliers. The first layer comprises 40 scintillators and is installed above the SM. The second one, comprising 50 scintillators is positioned below the SM in a way that the a particle passing the active area of all six layers in the SM on outermost particle track possible is detected by both layers of scintillators (see figure 4.2). The design results into a largest measurable angle α_{L} of the particle tracks of 26 ° with respect to the x, z-plane. The logic circuit sends a trigger-signal to the trigger logic of the SM in case of a coincidence of the signals from the two layers of scintillators (‘coincidence trigger‘).

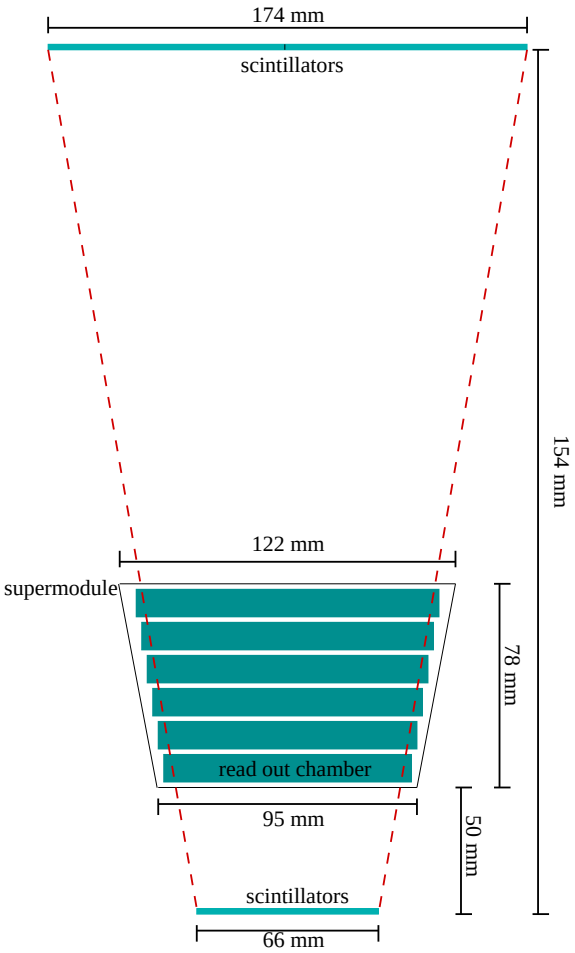

Figure 4.2: The cosmic trigger setup (illustration based on B. Bathen [Bat07]).

CHAPTER 5

Averaged Pulse Height Distributions

The temporal behaviour ('shape') of the signal in subsequent time bins, which is created as described in chapter 3.3.3, is influenced by several factors. To analyse the shape of the pulse height distribution the signal thatis taken on all pads, which are read out (compare with chapter 8), is averaged over many events. One event lasts 3 μs and has thus, because the ADC sampling rate is 10 MHz, 30 time bins with a duration of 0.1 μs each.
The resulting averaged pulse height distribution is geometrically determined by the ROC design and can be separated into four parts. The first part consists of the so-called presamples. They are taken before the primary particle has created a measurable signal in the ROC to avoid cutting off the onset of the signal. Thereby the time zero is arbitrarily set to 0.5 μs before the signal rises as it is displayed in figure 5.1.

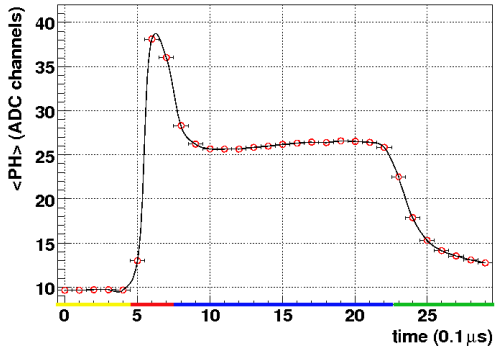

Figure 5.1: The averaged pulse height $\langle PH \rangle$ as a function of the drift time. It can be seperated into four parts: presamples (yellow), amplification peak (red), drift plateau (blue) and tail (green).

The peak at time bin six corresponds to the amplification region. On both sides of the anode wire plane, in front of the cathode wire plane and the pad plane on the other side, the primary particle ionises gas atoms. The resulting avalanches of those ionisation processes, which have the same distance to the anode wire plane on both sides, are sampled at the same time and thus contribute to the signal in the same time bin. The following plateau corresponds to the drift region. The electrons generated outside the amplification region drift to the cathode wire plane with a constant drift velocity because of the homogeneous electric field. They enter the amplification region at a constant rate. Since mainly muons are measured in the SM test setup, no TR is produced, whose conversions would be superimposed on the usual ionisation energy loss. In addition the electrons of the cosmic showers traverse the drift region first and afterwards the radiator in the SM test setup. Thereby, eventually produced TR is peaked forward to the bottom of the chamber instead of entering the drift region. Furthermore the ROCs are operated with an (Ar,CO_2) mixture instead of (Xe,CO_2), which is necessary to measure TR. All that leads to the fact that the drift plateau remains flat instead of rising due to TR at higher drift times.
The fourth part of the signal is the tail at the end of the drift plateau. It is due to the convolution of the signal from the ion tails and the finite response of the PASA.
Beside the ROC design the shape of the signal is influenced by the choice of the electric fields in the drift and in the amplification region.

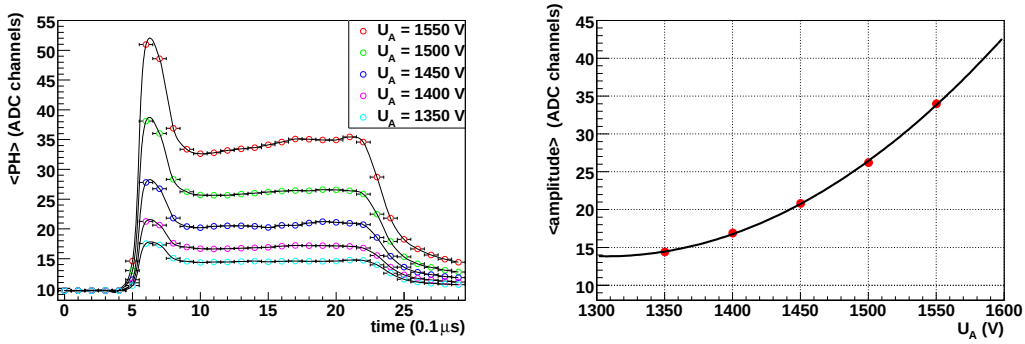

Figure 5.2: Averaged pulse height $\langle PH \rangle$ as a function of the drift time. Left panel: Pulse height for different anode voltages U_A and constant drift voltage U_D. The peak corresponds to the amplification region, whereas the plateau is due to the constant electric field of the drift region. The gas gain of the ROC is a function of the anode voltage. Thus varying the anode voltage leads to different pulse heights. The right panel shows the height of the drift plateau as a function of the anode voltage (red dots). The data is fit with a second degree polynomial function (black line).

In figure 5.2 and figure 5.3 the averaged pulse height distributions for various applied voltages are displayed. The left panel of figure 5.2 shows five distributions resulting from five different anode voltages U_A. The drift voltage U_D is held constant at 1250 V (E = 417 V/cm). Due to the rising gas gain, increasing U_A leads to a higher average signal. The

amplitude of the amplification peak as a function of the voltage U_A is shown in the right panel of figure 5.2.

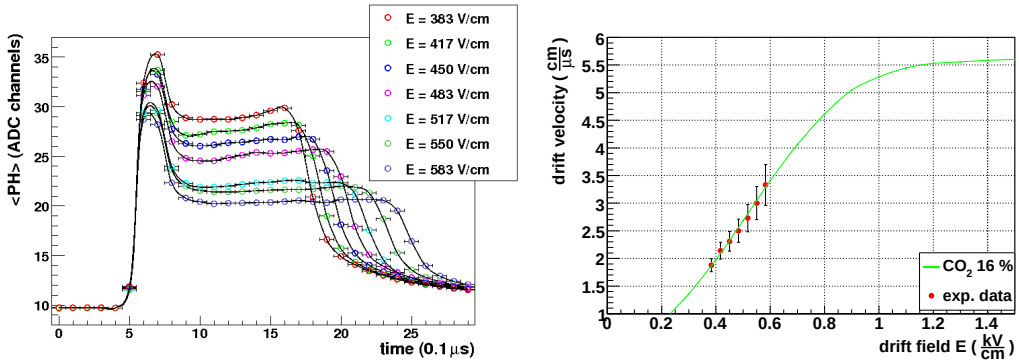

Figure 5.3: The left panel shows the average pulse height as a function of drift time for different electric fields ($U_A = 1500\,\mathrm{V}$). The height of the drift plateau rises with the applied voltage U_D as the same amount of ionisation electrons reaches the amplification region in shorter time. The length of the plateau equals the time the ionisation electrons need to traverse the drift region of 3 cm length. The arising drift velocity is plotted as a function of the electric field in the right panel and compared with a GARFIELD/MAGBOLTZ calculation for Ar, CO_2.

The effect of varying the drift voltage U_D is presented in the left panel of figure 5.3. The anode voltage is held constant at 1500 V. The drift velocity increases with higher voltages U_D and the ionisation electrons reach the amplification region in a shorter period of time. The length of the drift plateau corresponds to this drift time. With decreasing drift time the height of the plateau has to increase because the amount of ionisation electrons in the drift region remains constant but is collected by the detector in a shorter time.
The drift velocity of the electrons can be estimated roughly on the basis of the drift time determined by the length of the plateau and the known length of the drift region in the ROC. The results for seven different U_D are presented in table 5.1 and displayed in the right panel of figure 5.3.
The drift velocity is also a function of the gas mixture in the ROC. The presented results are taken with Ar,CO_2 (84.6/15.4). They are compared with a GARFIELD/MAGBOLTZ calculation [Bia99], [Vee98]. The ROC is operated in the region where the drift velocity is a linear function of the electric field for the applied voltages.
In the left panel of figure 5.3 not only the drift plateau increases at higher voltage but the amplification peak increases as well. This effect is due to the ROC geometry [Bus02]. The cathode wire plane does not completely isolate the drift region from the amplification region. The gaps between the wires are of the same order of magnitude as the distance from the cathode wire plane to the anode wire plane. As a consequence, the ground level equipotential surface is not located at the cathode wire plane, but extends into the drift region and thus the drift voltage U_D influences the sample behaviour of the amplification

E ($\frac{\mathrm{V}}{\mathrm{cm}}$)	time $\mathrm{bin}_{\mathrm{start}}$	time $\mathrm{bin}_{\mathrm{end}}$	drift velocity ($\frac{\mathrm{cm}}{\mu\mathrm{s}}$)
383	8	23	1.9
417	8	22	2.1
450	8	19	2.3
483	8	18	2.5
517	8	17	2.7
550	8	16	3.0
583	8	14	3.3

Table 5.1: The length of the drift plateau for different electric fields in the drift region and the resulting drift velocity.

region as well.
Unless mentioned otherwise the following analyses are accomplished with $U_D = 1250\,\mathrm{V}$, which corresponds to E = 417 V/cm, as a long drift plateau is desirable to get more data points. Further U_A is set to 1500 V, which is a comparatively high anode voltage, to achieve a good signal to noise ratio without running the risk of damaging the anode wire by a gas discharge.

CHAPTER 6

Position Resolution of the ROCs

The main tasks of the TRD are particle identification (PID) and particle tracking. For the former the shape of the signal, especially in those time bins which correspond to the drift region, is analysed to detect created transition radiation. For the latter purpose not the height of the signal but the distribution of the signal on adjacent pads of the pad plane in every single time bin is analysed. A charged particle crossing the detector, like electrons, pions and other hadrons at ALICE or muons at the test setup, creates a signal by gas ionisation as it is described in chapter 3.3.3. A so-called 'hit' is the signal distribution on adjacent pads on the cathode pad plane caused in one time bin. The position of the centre of a hit can be reconstructed with a resolution better than the pad width W (6.35 mm for L0-type chamber) using the PRF. In this chapter the PRF of the detector will be determined and the position resolution of the ROCs will be investigated.

6.1 Pad Response Function

Figure 6.1 shows a signal distribution recorded on the pad plane as a function of time after a particle originating from a cosmic ray (primary particle) has crossed the chamber along a certain trajectory. Illustrated is the signal of one event (over 30 time bins) on six pads adjacent in one row. The first five time bins are the pre-samples and in time bin five the amplification peak rises. From time bin eight on the signal originating from the electrons that are generated in the drift region is sampled. Because $Q_{i=66}(\mathrm{tb}=8)$ is of higher intensity compared with the two neighbouring pads Q_{i-1} and Q_{i+1}, it is called the centre pad of the hit. The effect that the created avalanches induce a signal on several adjacent pads is called 'charge sharing'. It provides the possibility of position reconstruction with a finer resolution than the width of a pad. In most cases a signal is distributed among three adjacent pads, which is called a '3-pad-cluster'. Less frequently 2-pad-clusters, 4-

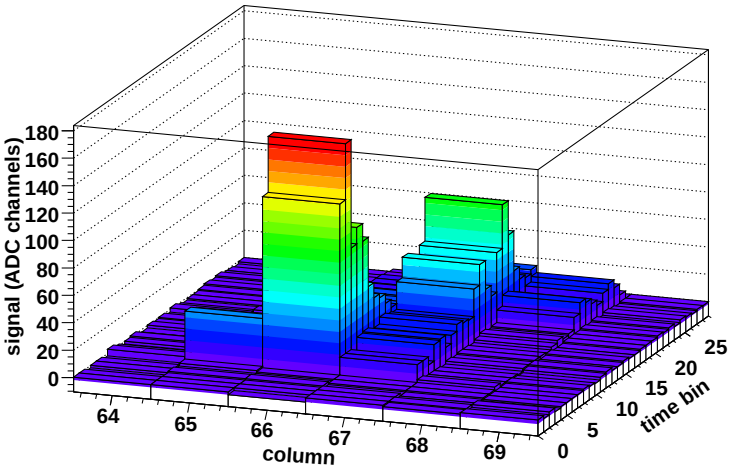

Figure 6.1: A signal distribution recorded on six adjacent pads in all 30 time bins of one event.

pad-clusters and 1-pad-clusters are created as well. In the following time bins the centre of gravity of the signal shifts to the right. This is due to the incident angle α of the primary particle with respect to the x,z-plane.
The signal distribution is used for one-dimensional position reconstruction in y-direction. In addition, the knowledge of the drift velocity of the ionisation electrons (see chapter 5) allows to reconstruct the position of the ionisation processes caused by the primary particle in the gas volume of the ROC in x-direction. As the distance of the ionisation processes from the anode wires corresponds to the arrival time and thus to the tbs, the ROCs offer a 2-dimensional reconstruction of the particle track.
The PRF is applied for position reconstruction using the signal distribution on the pad plane. It is defined as the ratio of that part of the signal which is induced on a single pad to the total induced signal as a function of the distance of the centre of the hit to the centre of the single pad in y-direction. In the following the 'displacement' y of a certain hit is defined as the distance of the centre of the hit to the centre of its centre pad.
If a Gaussian shape is assumed and if the total signal is approximated to be induced on three adjacent pads in one time bin, the PRF can be parametrised as follows [BR94]

$$PRF(y) = \frac{Q_{pad}}{Q_{tot}} = \frac{Q_i}{Q_{i-1} + Q_i + Q_{i+1}} = Ae^{-\frac{y^2}{2\sigma^2}} \quad . \tag{6.1}$$

A is the amplitude of the Gaussian function and σ is its variance. Thus the induced signal on three adjacent pads (i-1,i,i+1) caused by a hit having its centre at the displacement y is given by

$$Ae^{-\frac{(y+W)^2}{2\sigma^2}} = \frac{Q_{i-1}}{Q_{i-1}+Q_i+Q_{i+1}} \ , \tag{6.2}$$

$$Ae^{-\frac{y^2}{2\sigma^2}} = \frac{Q_i}{Q_{i-1}+Q_i+Q_{i+1}} \ , \tag{6.3}$$

$$Ae^{-\frac{(y-W)^2}{2\sigma^2}} = \frac{Q_{i+1}}{Q_{i-1}+Q_i+Q_{i+1}} \ , \tag{6.4}$$

where W is the pad width given in table 3.2. Without prior knowledge of the variance σ the displacement y has to be calculated using the signal distribution (Q_{i-1}, Q_i, Q_{i+1}). If equation 6.3 is divided by 6.2 and 6.4 by 6.3, it follows:

$$e^{-\frac{2yW+W^2}{2\sigma^2}} = \frac{Q_i}{Q_{i-1}} \ ,$$

$$e^{-\frac{2yW-W^2}{2\sigma^2}} = \frac{Q_{i+1}}{Q_i} \ ,$$

and consequently

$$e^{-\frac{2yW}{\sigma^2}} = \frac{Q_{i+1}}{Q_{i-1}} \ , \tag{6.5}$$

$$e^{-\frac{W^2}{\sigma^2}} = \frac{Q_i^2}{Q_{i-1}Q_{i+1}} \ . \tag{6.6}$$

By insertion of 6.6 in 6.5 and solving for y an expression for y is found, which is independent of σ

$$y = \frac{W}{2}\frac{\ln(Q_{i+1}/Q_{i-1})}{\ln(Q_i^2/Q_{i-1}Q_{i+1})} \ . \tag{6.7}$$

For 10^6 events y and PRF(y) have been calculated using equations 6.7 and 6.1. The results are shown in the left panel of figure 6.2. In the right panel the mean of each channel is indicated as a dot and a Gaussian fit is applied. The Gaussian fit agrees well with the measured data in the region of the centre pad i up to the centre of the neighbouring pads at (y = -1, y = 1). Beyond that, the fit diverges slightly from the measured PRF (dots). As it is described in chapter 3.3.3 the PRF can be calculated using the Mathieson formula, which is a single parameter expression. The parameter K_3 is a function of the radius of the anode wires, the gap between the anode wires and the distance from the anode wires

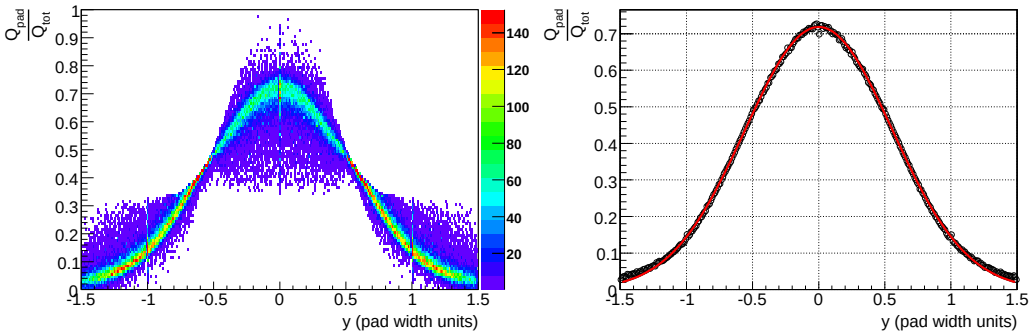

Figure 6.2: The measured Pad Response Function of a L2-type ROC (padwidth W = 6.95 mm). Left panel: The scatter plot gives the counts of the measured PRF(y) for y ϵ [-1.5, 1.5]. Right panel: The mean of each channel is plotted as a dot. The red line represents a Gaussian fit to the measured PRF.

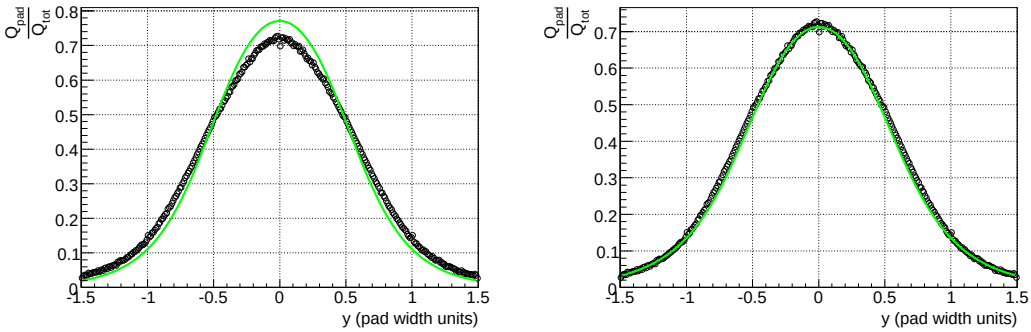

Figure 6.3: The left panel shows the measured PRF (dots) and the calculated PRF using the Mathieson formula ($K_3 = 0.67$). It is evident, that the calculated function does not agree with the measured PRF, which is considerably broader. That is due to crosstalk between adjacent pads. The right panel shows the Mathieson formula for the case $K_3 = 1.15$. It is in better agreement with the measured data.

to one cathode plane. In the left panel of figure 6.3 the calculated PRF is compared with the measured PRF, which is considerably broader than the calculated one. This is a consequence arising out of the crosstalk between adjacent pads [tdr01]. In spite of that, the measured PRF can be fit well with the Mathieson formula if K_3 is not restricted to one certain value. Due to the not ideal behaviour of the electronics, the parameter K_3 then takes a value outside its domain of definition [0,1]. Accounting for that, the measured PRF can be well described especially in the region beyond the centres of the neighbouring pads where the Gaussian fit deviates from the measured PRF.

As the six different ROC-types have the same distance of the anode wires to the pad plane but different pad widths, their PRFs look different. The PRFs of all six layers and thus ROC-types are plotted in the left panel of figure 6.4. The right panel presents σ as an approximate linear function of the pad width W, which is a linear function of the layer

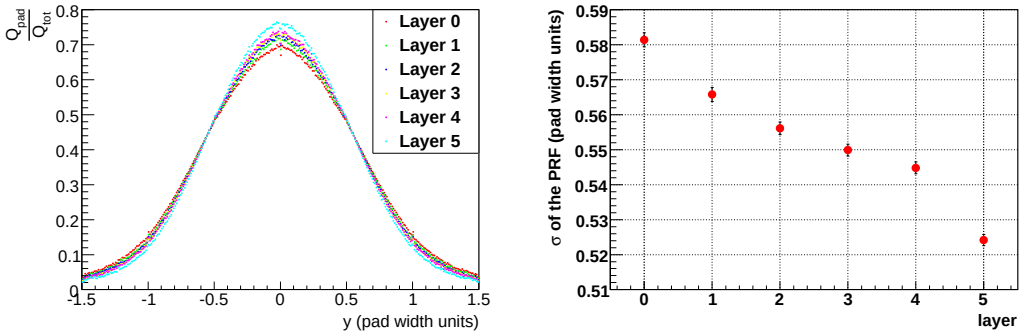

Figure 6.4: Since the PRF is a function of the ratio of the distance of the anode wires and the pad plane to the padwidth, it has a different shape for each ROC-type (left panel). The variance σ of each type is plotted against the corresponding layer number (right panel).

number. In the following the variance σ determined for the PRF is used to calculate the displacement y of a hit with respect to the centre of the pad, on which the most charge is induced in the first time bin of the drift plateau.

6.2 Offline Position Reconstruction

If the variance σ of the Gaussian fit of the PRF is known, the displacement y can be determined in case of a 2-pad-cluster using

$$y = \frac{\sigma^2}{W} \ln \frac{Q_i}{Q_{i-1}} - \frac{W}{2} \tag{6.8}$$

or

$$y = \frac{\sigma^2}{W} \ln \frac{Q_{i+1}}{Q_i} + \frac{W}{2} \ . \tag{6.9}$$

In the case of a 3-pad-cluster the combination of these two to a weighted average with the weights w_1 and w_2 is applied

$$y = \frac{1}{w_1 + w_2} (w_1 \cdot (-\frac{W}{2} + \frac{\sigma^2}{W} \ln \frac{Q_i}{Q_{i-1}}) + w_2 (\frac{W}{2} + \frac{\sigma^2}{W} \ln \frac{Q_{i+1}}{Q_i})) \ . \tag{6.10}$$

Since the errors of charge measurement are approximately inverse to the amount of charge which is induced on the pad, the error of the displacement calculation can be minimized if the weights are choosen as $w_1 = Q_{i-1}^2$ and $w_2 = Q_{i+1}^2$ [BR94]. The displacement y of a hit is now reconstructed for every time bin of the drift plateau. A linear fit shows the mean displacement along the y-axis of the pad plane per unit of time. As the signal in every time bin corresponds to the electrons originating from ionisation processes at a certain distance

from the anode wires the slope c of the linear fit of y(tb) corresponds to the incident angle α of the primary particle (see illustration 6.5).

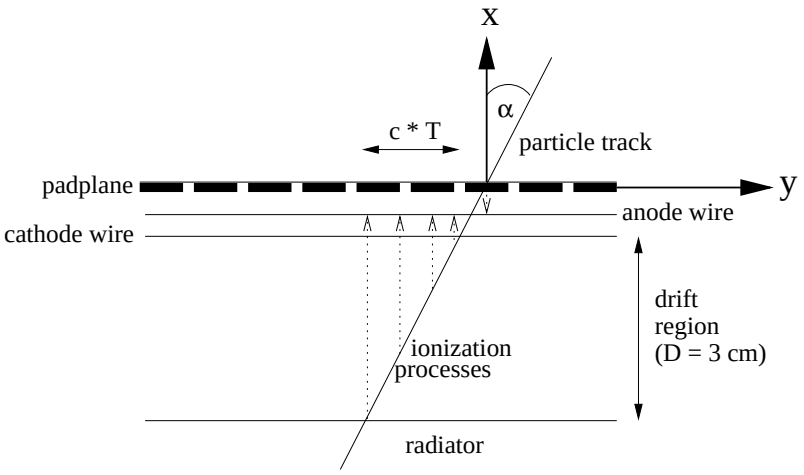

Figure 6.5: Cross section through a ROC. A particle hits the ROC with an incident angle α. The electrons resulting from ionisation processes in the drift region and the amplification region move to the anode wires and create avalanches, which are detected on the pad plane. The length $(c \cdot T)$ of the affected area of the pad plane during the drift time T is a function of the angle α.

For $\alpha \neq 0°$ the ionisation electrons from different parts of the track arrive at different displacement coordinates, whereas at $\alpha = 0°$ the signal distribution is induced on the same adjacent pads in every tb. In that case the position of the hit is also reconstructed at the same position in every time bin and thus the slope c is 0 mm/tb. With T being the drift time and D the depth of the drift region α is given by

$$\tan\alpha = \frac{c \cdot T}{D} \ . \tag{6.11}$$

One SM consists of six layers of five ROCs each. Thus the passing cosmic ray particles induce a signal in up to six ROCs in one event. Figure 6.6 shows the calculated displacement in all time bins of the drift plateau in the six ROCs, which have been hit by one particle and the appropriate linear fit ($y_{\text{fit}} = a + c \cdot \text{tb}$).

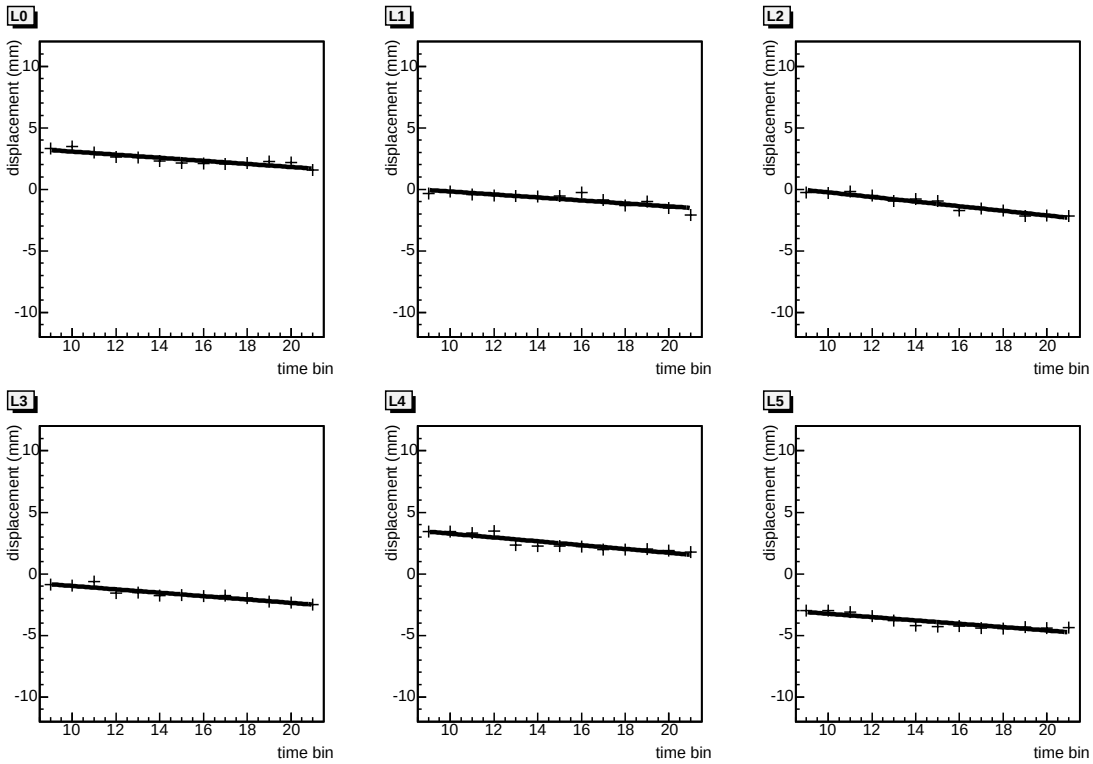

Figure 6.6: The tracks of one particle crossing six overlying ROCs. Shown is the displacement y from the centre of the central pad as a function of the time bin number calculated for all time bins corresponding to the drift plateau.

6.3 Position Resolution Performance

In this chapter the resolution of the position reconstruction is determined without using any external tracking device. Therefore, the residuals Δ_y of a given track in one ROC are defined as the distance between the reconstructed displacement y_{rec} and the value of the fit in the according time bin y_{fit}

$$\Delta_y = y_{\text{rec}} - y_{\text{fit}} \ . \tag{6.12}$$

Then the position resolution of a detector σ_{pos} is defined as the variance σ of the Gaussian fit of the distribution of residuals Δ_y for a large number of tracks. The left panel of figure 6.7 shows the distribution of residuals for a L0-type ROC. Overlapping hits, which originate from different primary particles, lead to an erroneous position reconstruction and thus to a decline of the position resolution σ_{pos}. To avoid this, all hits are rejected that do not fulfil a condition called the 'Cluster Quality Cut' before the calculation of the residuals takes place. The applied threshold T_Q is calibrated in section 7.2 'Calibration of the Cluster Quality Cut'.
Since the resolution is a function of the pad width given by the ROC-type (see table 3.2), the resolution has to be determined for every ROC-type individually. Like the pad width, the resolution is supposed to be a linear function of the layer number. The result of the calculation of the resolution for all six ROC-types shows an approximately linear relationship and thus agrees well with the expected results (see right panel of figure 6.7).

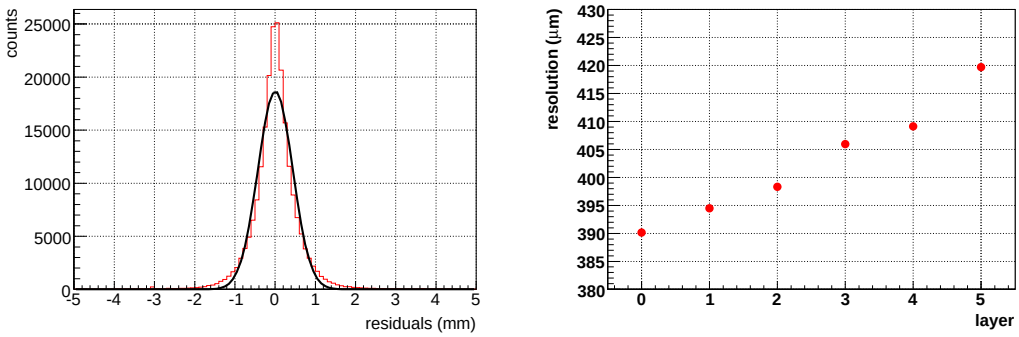

Figure 6.7: Left panel: Residuals of a L0-type ROC calculated for 10^6 events. The variance of a Gaussian fit (black line) to the residual distribution (red line) is defined as the position resolution of the ROC. Right panel: The position resolution of each ROC-type in μm as a function of the layer number.

The exact values of the position resolution for all six ROC-types are presented in table 6.1.

Layer	Position Resolution (μm)
0	389.1 ± 1.0
1	394.8 ± 1.0
2	399.6 ± 1.0
3	404.6 ± 1.0
4	408.9 ± 1.0
5	418.7 ± 1.0

Table 6.1: The values of the position resolution σ_{pos} and the uncertainty of the variance of the Gaussian fit for all six ROC-types.

The values given in table 6.1 are averaged over all angles of incidence α of the primary particle. But in addition to the ROC-type, the position resolution σ_{pos} is a function of α as well.
The reconstructed position of the ionisation process in the drift volume of the ROC has uncertainties in x-direction and in y-direction. The position resolution in y-direction σ_{y} is determined by the ROC geometry. The position resolution in x-direction σ_{x} is determined by the distribution the charge that is deposited by the primary particle within the range s_{tb}. This is the distance, which the ionisation electrons travel towards the amplification region in one time bin with the drift velocity v_{drift} (see illustration 6.8).

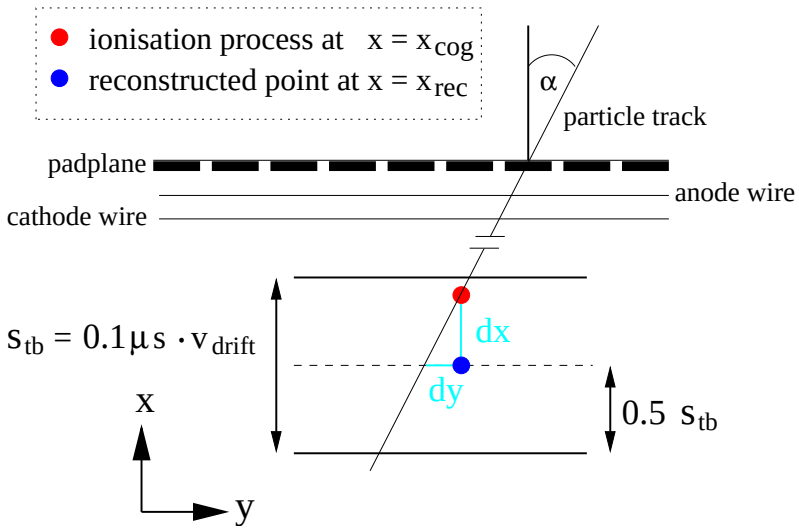

Figure 6.8: s_{tb} is the length of the distance the ionisation electrons travels towards the amplification region in one time bin and dy is the uncertainty in y-direction resulting from σ_{x}.

dx is the distance in x-direction between the centre of gravity of the deposited charge at x_{cog} and the point where it is reconstructed at x_{rec} due to its time bin information. This results into a deviation in y-direction dy of the reconstructed point from the particle track in the according time bin due to the uncertainty in x-direction. $\sigma_{\mathrm{x}\to\mathrm{y}}$ is the width of the dy distribution and given by

$$\sigma_{\mathrm{x}\to\mathrm{y}} = \sigma_x \cdot \tan\alpha. \tag{6.13}$$

Thus the influence of σ_{x}, which is given by $\sigma_{\mathrm{x}\to\mathrm{y}}$, on the total position resolution in y-direction σ_{pos} is a function of the incident angle α

$$\sigma_{pos} = \sqrt{\sigma_{\mathrm{x}\to\mathrm{y}} + \sigma_{\mathrm{y}}} = \sqrt{\sigma_x \cdot \tan\alpha + \sigma_y}. \tag{6.14}$$

In figure 6.9 the resolution σ_{pos} of a L0-type ROC as a function of α is presented and fit according to equation 6.14. The analysis is made with data taken with by-passed tail cancellation filter. Since the ion tails lead to an erroneous angle reconstruction (see section 6.4), reliable values of σ_{x} and σ_{y} can be determined as function of the layer number once the set of TC parameters is recalibrated.

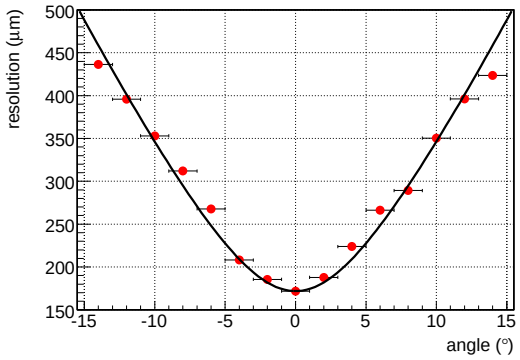

Figure 6.9: The measured resolution of a L0-type ROC in micrometer as a function of the reconstructed incident angle α. The black line is a fit according to $\sigma_{pos} = \sqrt{\sigma_{\mathrm{x}\to\mathrm{y}} + \sigma_{\mathrm{y}}}$ with $\sigma_{\mathrm{x}} = 1510\,\mu\mathrm{m} \pm 103\,\mu\mathrm{m}$ and $\sigma_{\mathrm{y}} = 186.9\,\mu\mathrm{m} \pm 0.7\,\mu\mathrm{m}$

6.4 Influence of the Ion Tails on the Resolution

Due to the ion tails a signal in one time bin always creates a signal on the same pad in the subsequent time bins as well. The ions induce a charge on the pad plane in the time bin according to the moment of their creation in the avalanche. During their drift to the pad plane of several microseconds duration they induce a signal in the following tbs. The resulting strong correlation among subsequent time bins, convoluted with the

PASA response, leads to a rigorous influence of the ion tails on the angular resolution performance.
As it is mentioned in chapter 3.3.4 the ROCs are able to perform tail cancellation (TC) as part of the implemented online filtering. The set of parameters of the filter has been choosen to be [A+05]:

$$\begin{aligned} 246 &= [\alpha_{\mathrm{L}} \cdot 2^{11}] \\ 285 &= [(\lambda_{\mathrm{L}} - 0.75) \cdot 2^{11}] \\ 211 &= [(\lambda_{\mathrm{S}} - 0.75) \cdot 2^{11}] \end{aligned} \tag{6.15}$$

The effect of the tail cancellation on the shape of the signal is presented in figure 6.10. The data presented in the left panel is taken with no applied drift voltage. Hence the ionisation electrons from the drift region do not reach the amplification region and the pulse height plot only shows the amplification peak. The data taken with by-passed tail cancellation filter (no-TC) show the ion tail on the falling edge of the peak. They have considerably higher values in all time bins compared with the data taken with TC. In the TC data the peak is more symmetric and lasts three time bins, after which it returns to the baseline. In contrast to that, the signal of the no-TC data does not return to the baseline within the 30 time bins as it takes the ions several microseconds until they arrive at the pad plane. It is clear to see that the ions, which are created in avalanches near time bin six, influence the measurement on the according pads in the subsequent time bins.
The right panel shows the averaged pulse height plots for TC and no-TC data for the case that anode voltage and drift voltage are applied. The height of the amplification peak stays approximately the same if TC is applied. The small deviation indicates that with the chosen set of parameters the effect of the TC is a little bit too strong. Therefrom also arises the small undershoot between the amplification peak and the drift plateau. The drift plateau is the part of the signal most strongly affected by the TC. In the no-TC data the plateau is slightly rising due to the fact that the ion tails created in the previous time bins are all added up. In the TC-data the plateau is flat. In addition, the height of the plateau has been decreased by approximately 50 %. A decrease of about 30 % is expected (see [Bus02]). The deviation is another indicator that the parameters have to be recalibrated.
In the following, the effect of the ion tails on the angular resolution is analysed. A signal on one pad in an early time bin leads to an increased signal on that pad in the following time bins because of the slow drift velocity of the created ions. Due to an angle of incidence α ($\alpha \neq 0°$) the centre of a hit it shifted on the pad plane in subsequent time bins and thus a signal is induced on different adjacent pads in different time bins. The signal on those pads, which have been hit first, is higher in the later time bins than it should be with respect

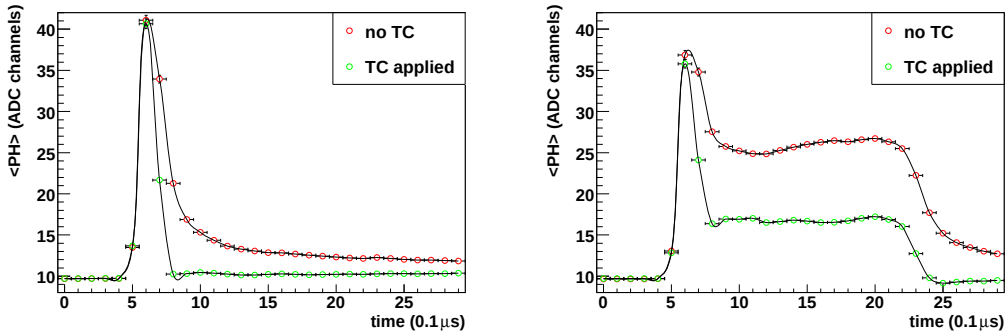

Figure 6.10: Average pulse height distributions of data taken with TC (green dots) and without TC (red dots). In the left panel no drift voltage is applied and therefore the plot only consists of the amplification peak. The right panel shows the shape of the signal if anode voltage and drift voltage are applied.

to the position of the avalanches because the ion tails of the former avalanches are still recorded. Therefore, the reconstructed angle with respect to the x, z-plane is too small compared with the corresponding incident angle. The distribution of all reconstructed angles in the six ROCs of one stack in 10^6 events is presented in the left panel of figure 6.11. Obviously, the angles that are reconstructed when no TC is applied, are smaller compared with the angles that are reconstructed when the data is filtered.

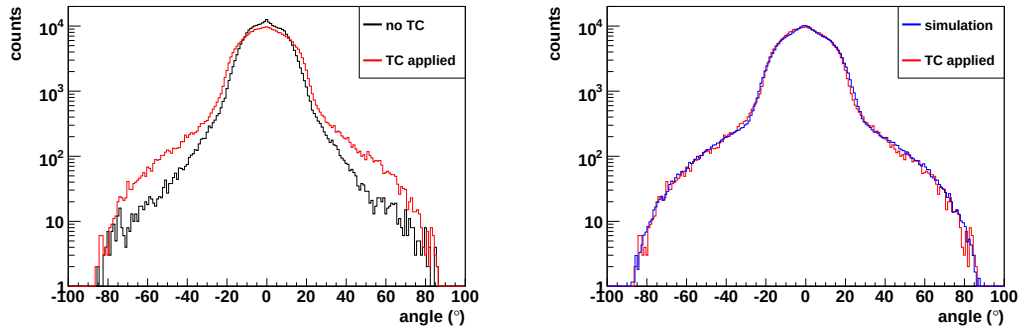

Figure 6.11: The reconstructed angle distribution of six ROCs in 10^6 events. Left panel: The distribution corresponding to the no-TC data (black curve) is narrower than the distribution corresponding to the TC data (red curve) because the ion tails lead to the effect that angles are reconstructed too small if no TC is applied. Right panel: The distribution of the filtered data (red curve) is compared with a simulation (blue curve) of the angle distribution if the ratio between tracks that are triggered with the coincidence trigger and additional recorded tracks is 83:17 [Bat09].

The right panel of figure 6.11 shows the the measured angle distribution if TC is applied and a simulated angle distribution of tracks crossing the SM based on an overall angular distribution of muons $\propto \cos^2 \Theta$ [Bat09]. The largest angle of a track with respect to the

x, z-plane that can lead to a coincidence of the signals from the two layers of scintillators of the cosmic trigger setup α_{L} is 26 ° But since the the whole SM is read out in case of a trigger signal, non-triggered tracks can additionally be recorded. Because of that, angles higher than α_{L} are reconstructed as well. The presented simulation is based on a ratio of tracks that are triggered with the coincidence trigger and additional recorded tracks that allow $|\alpha| \geq 26\,^{\circ}$ of 83:17. In addition, a Gaussian smearing of 3.0 ADC channels is assumed.

The described effect of angles that are reconstructed too small in case of a by-passed TC filter can be specified by analysing the shape of the single event signal. The higher a recorded signal in one time bin, the stronger is the influence of its ion tail in the subsequent time bins. In addition, the ion tails caused in an earlier time bin influence more subsequent time bins than ion tails attributed to a later time bin. Consequently, the reconstructed angles are a function of the centre of gravity in time t_{cog} of the recorded signal. In figure 6.12 the distributions of the reconstructed angles for different t_{cog} normalised to the number of tracklets are shown. In the left panel the results for no-TC data is presented. The earlier t_{cog} is placed, the smaller the distribution of reconstructed angles around 0°. That means that in case of events with high signals in early time bins the reconstructed angles are systematically smaller. The effect is no longer present in the right panel, where the filtered data is presented.

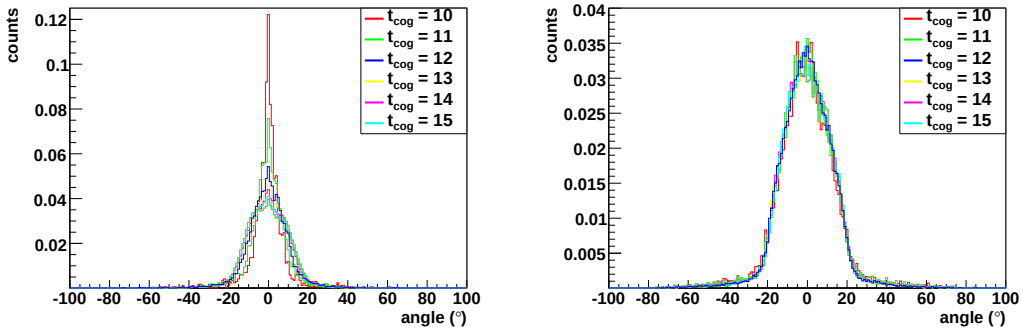

Figure 6.12: The distributions of reconstructed angles for different t_{cog} normalised to the number of tracks. Left panel: no TC has been applied while data taking and the width of the distribution is a function of t_{cog}. Right panel: the data was taken with TC and thus no correlation between the position of t_{cog} and the width of the distribution is observable.

CHAPTER 7

Online Position Reconstruction

In chapter 3.3.4 it is described that already during the readout of each event the position of the hits and the resulting tracklets are calculated. That online tracking enables the TRD to provide a trigger decision within 6.5 μs because the electron probability is calculated online as well. In this chapter it is presented how the displacement y of a hit is calculated in the TPP and needed parameters are calibrated.

7.1 Displacement Calculation in the TPP

Expression 6.10 given in chapter 6.2 for the displacement calculation is rather long and includes several arithmetic operations. To decrease the expense of gates in the arithmetic unit of the TPP, the online position reconstruction differs from the offline position reconstruction. The arithmetic units get the hit information from the hit selection unit to calculate the fitsums as it is described in chapter 3.3.4. The information includes the centre pad $Q_i(tb)$ = C, the left neighbour $Q_{i-1}(tb)$ = L and the right neighbour $Q_{i+1}(tb)$ = R. For the following calculation the baseline value added before by the pedestal filter is substracted first (see illustration 7.1).

Whereas in the offline position reconstruction the PRF is used to find the displacement of a hit to the centre of pad i, the TPP calculates the expression [Gut06]

$$\overline{COG} = \frac{R - L}{C}, \tag{7.1}$$

which differs slightly from the Center-Of-Gravity (COG) calculation

$$COG = \frac{R - L}{R + C + L} \ . \tag{7.2}$$

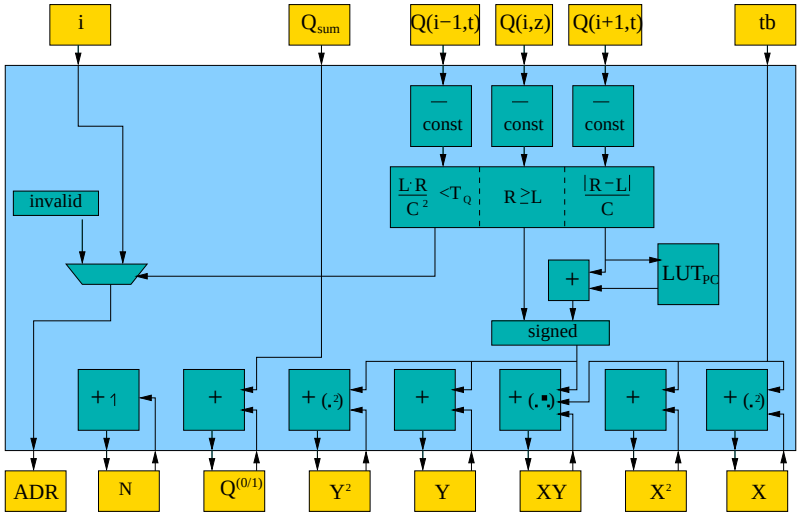

Figure 7.1: The arithmetic unit in the TPP. The hit information is used to calculate the fitsums (based on [Gut06]).

The quantity $y^{\text{est}} = \frac{1}{2}\overline{COG}$ is the first estimation of the displacement. In figure 7.2 y^{est} is plotted as a function of $\overline{COG}$ together with the displacement y, which is calculated using the PRF. The deviation from y to y^{est} is only positive and the relationship between the two quantities is unique. Hence there exists a one-to-one transformation from y^{est} to y that is used for a correction of the calculated y^{est}, which is done via a LUT with 128 positive entries. These entries have to be calibrated using the measured PRF of the detector. They consist of 5 bits each and give the deviation in $\frac{1}{256}$ pad width units. That results into an accuracy better than 2^{-8} pad widths. As the LUT entry is restrictet to 5 bits, the maximal possible value is $\frac{31}{256}$ pad width units. The calculated deviation goes up to $\frac{24}{256}$ pad width units in layer five. In that case the deviation of y^{est} to y, which is corrected by the LUT, amounts to 740 μm.

Since the PRF is symmetric the calculation is done for $|y^{\text{est}}|$. The algebraic sign is gained from a comparison of the two neighbours and added to the resulting $|y|$.
The first step to determine $|y|$ is to calculate $\overline{COG} = 2 \cdot |y^{\text{est}}| = \frac{|R-L|}{C}$. Because of the earlier passed hit detection unit the result is between 0 and 1. It consists of 1 bit before and 7 bits after the decimal point. In the second step those 7 bits choose the corresponding 5 bit LUT entry. Afterwards $2 \cdot |y^{\text{est}}|$ is divided by two and the result is given by 8 bits after the decimal point, which are added to the 5 bit LUT entry. Thereby the 5 bits of the entry represent the bits from the fourth to the eighth position after the decimal point. Thus $|y|$ is given by

$$|y| = \frac{1}{2} \cdot 2 \cdot |y^{\text{est}}| + LUT(|2 \cdot y^{\text{est}}|) \; . \tag{7.3}$$

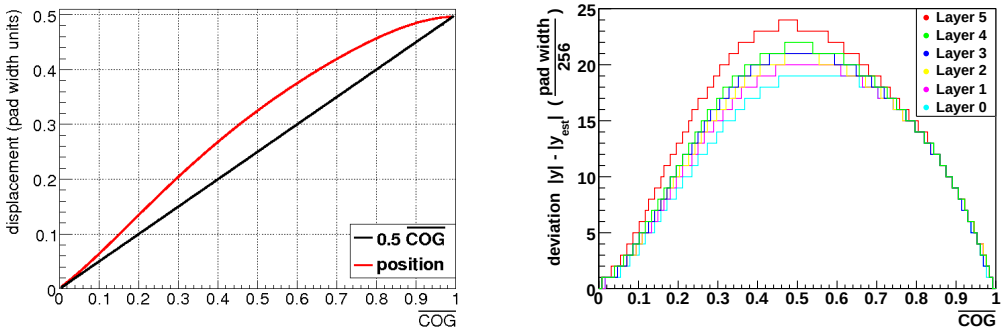

Figure 7.2: The left panel shows $y^{\text{est}} = \frac{1}{2}\overline{COG}$ and the displacement y calculated with the PRF as a function of $\overline{COG}$. The deviation is only positive and the relationship is unique. The right panel shows the deviation in $\frac{1}{256}$ pad width units for all six ROC-types.

The resulting y is the displacement of the hit from the centre of the pad in $\frac{1}{256} \approx 3.90 \cdot 10^{-3}$ pad width units. That is much better than the effective resolution of all six ROC-types (see chapter 6.2). The resolution is determined by the not ideal behaviour of the detector and digitisation effects in the ADCs.
To calibrate the entries of the LUT, the deviation $|y| - |y^{\text{est}}|$ is calculated for each layer as a function of $\overline{COG}$ with a granularity of 2^{-7} in the range [0,1]. The values of the entries of the six LUTs, each of them corresponding to one of the six ROC-types, are given in the right panel of figure 7.2.

7.2 Calibration of the Cluster Quality Cut

There is the possibility that the tracks of two particles in the detector get very close to one another or even cross each other so that the signal distributions (hits) caused by the two particles on the pad plane overlap (see illustration 7.3).
In that case the position reconstruction fails. Thus these incidents have a big influence on the position resolution performance of the detector and they lead to an erroneous tracklet calculation in the TP. To avoid that, a quality criterion called ‘Cluster Quality Cut‘ (CQC) is implemented in the TPP. If two hits are overlapping, the charge placed on the neighbour pads i+1 and i-1 of the centre pad i of a detected hit can be considerably higher than it is expected from the charge distribution given by the PRF. Hence the CQC looks like

$$T_Q > \frac{L \cdot R}{C^2} = \theta \ . \tag{7.4}$$

If the value θ exceeds the threshold T_Q, the arithmetic unit writes an invalid address to the fit register file and the hit is discarded. To calibrate T_Q the behaviour of the quantity θ is analysed. As the PRF looks different in each of the six ROC-types, T_Q has to be

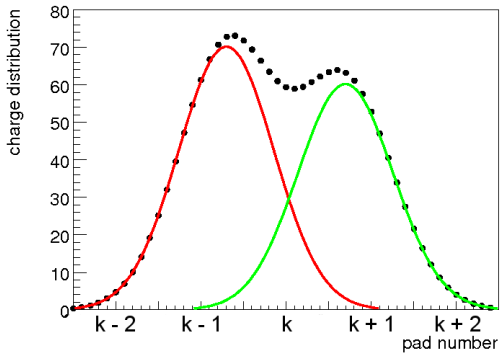

Figure 7.3: Two overlapping hits induce a signal distribution on the pad plane, which is misinterpreted as two hits with each of them having a too high signal on one neighbour pad k. Thus the displacement y is shifted to the region of overlap of the two hits.

calibrated individually for each ROC-type. If the PRF had an exact Gaussian shape, θ would be a constant value for each layer. But, as it is described in capter 6.1, the measured PRF deviates from the Gaussian fit in the region beyond the centre of the neighbour pads. Therefrom, θ is a function of the displacement y of the hit with respect to the centre of pad i. The left panel of figure 7.4 shows the measured PRF of a L0-type ROC and the right panel shows the resulting θ as a function of y.

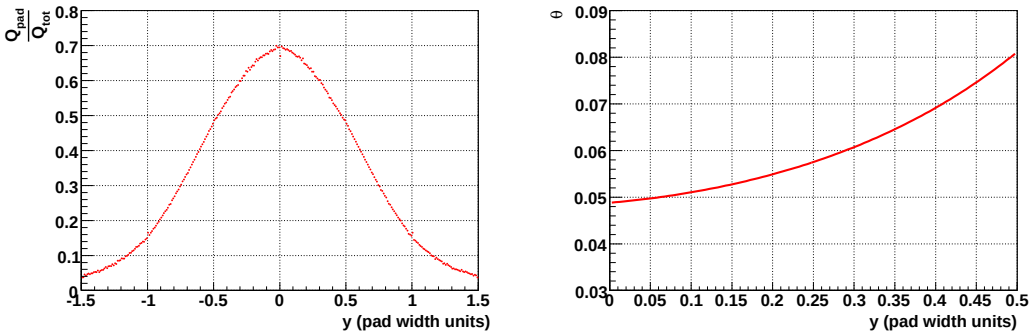

Figure 7.4: Left panel: The measured PRF of a L0-type ROC. Right panel: θ as a function of the displacement y. Because of the deviation of the measured PRF from a Gaussian shape θ increases with rising y.

The closer the centre of a hit gets to the border between two pads, the higher becomes θ up to a value $\theta_{\max}$ at $|y| = 0.5$. To keep all the valid clusters, T_Q has to be chosen at least higher than $\theta_{\max}$. The values of $\theta_{\max}$ for each ROC-type are presented in table 7.1. Since the errors of charge measurement are approximately inverse to the amount of deposited charge, the error of θ also rises the closer $|y|$ gets to 0.5. There the relative error of θ is

dominated by the relative error of the charge measurement on the small neighbour pad i_{small} and can be approximated as follows:

$$\frac{\Delta\theta}{\theta} = \frac{\sigma}{B \cdot i_{\text{small}}} \tag{7.5}$$

And thus, in order to keep all the valid clusters, T_Q has to be chosen such that:

$$T_Q = \theta_{\max} \cdot (1 + \frac{\sigma}{B \cdot i_{\text{small}}}) \tag{7.6}$$

where B is the minimum total cluster charge and σ the noise level. The noise level can be denoted with 1.1 ADC channels. In table 7.1 the resulting values of T_Q are presented, if B is chosen to be 20 ADC channels above baseline. This corresponds to a loss of true hits originating from a passing particle of 0.068 % (see chapter 8.1).

Layer	Θ_{max}	$Q_{n,small}$	T_Q
0	0.0811	0.0387	0.1859
1	0.0723	0.0347	0.1765
2	0.0669	0.0322	0.1708
3	0.0624	0.0301	0.1661
4	0.0603	0.0291	0.1639
5	0.0481	0.0233	0.1513

Table 7.1: The value of Θ_{max} at |y| = 0.5 and the resulting threshold T_Q for all six ROC-types.

In order to analyse how many hits are sorted out with the respective T_Q, the distribution of θ from 10^6 events for a L0-type ROC is calculated and presented in the left panel of figure 7.5. The θ distribution can be fit with a Landau distribution with a most probable value of 0.025. That differs from the calculated values of θ presented in 7.4 between 0.048 and 0.080. This is a covariance effect because $Q_i(tb)$, $Q_{i-1}(tb)$ and $Q_{i+1}(tb)$ are strongly correlated. Whereas in 7.4 $\langle \frac{Q_{i-1} \cdot Q_{i+1}}{Q_i^2} \rangle$ is calculated, the most probable value of the distribution in the left panel of figure 7.5 corresponds to the calculation of $\frac{<Q_{i-1}> \cdot <Q_{i+1}>}{<Q_i^2>}$. The right panel presents the ratio of hits that are kept to the total amount of hits if the thresholds T_Q are used, which are given in table 7.1.

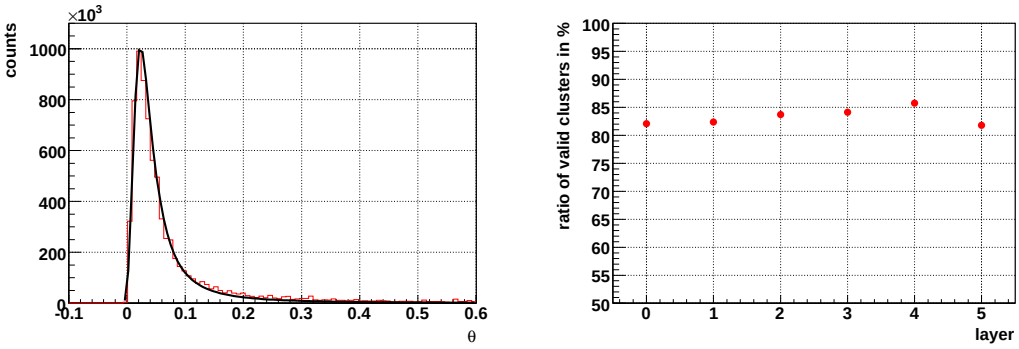

Figure 7.5: The left panel presents the distribution of θ for 10^6 events in a L0-type ROC together with a fit Landau distribution. The right panel shows the ratio of hits, whose Θ fulfil condition 7.2 and which thus are kept for the following calculations to the total amount of hits in %.

CHAPTER 8

Calibration of Zero Suppression in the Event Buffer

By ionising the gas mixture in the ROC, crossing particles deposit charge on the pads of the cathode pad plane in the vivinity of their passage (compare chapter 3.3.3). Since in each event there are many pads that do not receive any charge originating from a crossing particle, on many pads no important information will be stored. Therefore, there is no need to increase the amount of data by reading out all channels in every event. To ignore pads that contain only fluctuations around the baseline ('noise pads'), zero suppression (ZS) is applied. Thereby the employment of mass storage and the readout time can be optimised.
In this chapter the set of criteria that is provided by the TRAP (compare chapter 3.3.4) for the ZS is calibrated. For this purpose, the distribution of the noise and of the signal level as well as the event size as a function of the thresholds T_{IS} and T_{IT} are investigated. The danger arising from data compression is the possibility of losing important information. If pads on which some part of the produced charge is deposited are rejected the position reconstruction might become erroneous. This is why the effect of the zero suppression on the resolution has to be studied.

8.1 Calibration of the Single Hit Threshold (T_{IS}) and the Cluster Hit Threshold (T_{IT})

The pads of the cathode plane are capacitors with a capacitance of about $C_{\mathrm{pad-ground}} \approx 6\,\mathrm{pF}$ and thus show fluctuations around zero in their charge ('noise'). These fluctuations are amplified by the PASA, whose electronic noise was measured to be below 1200 electrons, and sampled by the ADC. To obtain the Root Mean Square (RMS) of the charge fluctuations in ADC channels, two different procedures can be applied.
The first one employs a so-called random trigger instead of the coincidence trigger de-

scribed in chapter 4. This way mainly noise is sampled. But if U_A remains high enough to provide avalanche creation in the amplification region, some signals originating from the cosmic particles are accidentally sampled as well.
In the second procedure U_A is set to zero to avoid gas amplification and thus only noise is sampled. In that case both trigger systems can be used, the coincidence trigger and the random trigger. But since U_A influences the noise behaviour of the pads, the result of this procedure ($U_A = 0\,\mathrm{V}$) is not in exact agreement with the noise distribution in ordinary data taking ($U_A = 1500\,\mathrm{V}$). Figure 8.1 shows the result of a noise measurement with the latter procedure.

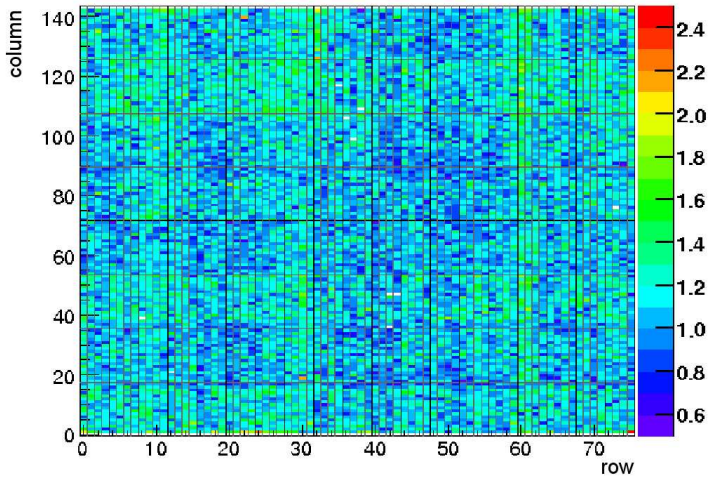

Figure 8.1: The RMS in ADC channels of the fluctuation of the signal around the baseline ('noise') of all pads of one layer measured with a coincidence trigger and $U_A = 0\,\mathrm{V}$.

As described in chapter 3.3.4, a set of indicator bits is used to select the pads that are supposed to carry a part of a true signal created by a passing particle. To minimise the event size, the least possible pads, which are not a part of a hit, have to be marked for readout. At the same time it is required that no true hits are lost due to the ZS. Therefore, the two thresholds T_{IS} and T_{IT} have to be calibrated, which have to be reaches by $Q_i(tb)$ and $Q_{i,sum}(tb) = Q_{i-1}(tb) + Q_i(tb) + Q_{i+1}(tb)$ respectively.
A pad is read out in all 30 time bins of one event if $Q_i(tb)$ reaches T_{IS} in at least one time bin of that event. Therefore, the determining quantity is the highest value that $Q_i(tb)$ reaches during the event. That maximum value is called $Q_{i,max}$. Analogous the pad is read out if the sum of the charge deposited on itself and on its two neighbouring pads $Q_{i,sum}(tb)$ reaches T_{IT} in one time bin. Hence $Q_{i,sum,max}$ is defined as the highest value that $Q_{i,sum}(tb)$ reaches during the 30 time bins.

The charge deposited on one pad i in all 30 time bins is called $tbsum_i$

$$tbsum_i = \sum_{tb=0}^{29} Q_i(tb). \tag{8.1}$$

In the following it is assumed that a particle crossing the detector always causes a local maximum in $tbsum_i$

$$tbsum_{i-1} < tbsum_i \geq tbsum_{i-1} \tag{8.2}$$

where pad i is called the central pad of the hit. It is important to note that also in regions with no true hits local maxima in $tbsum_i$ are recorded.
To determine how many pads that contain only noise ('noise pads') are expected to be read out as a function of the used threshold, the distributions of $Q_{i,max}$ and $Q_{i,sum,max}$ in ADC channels above baseline are investigated. The data is taken from $2 \cdot 10^4$ events with $U_A = 0\,\mathrm{V}$. Due to the lack of amplification voltage, the recorded signal originates exclusively from the fluctuations of charge on the pads. Figure 8.2 shows the measured distribution of $Q_{i,max}$ and $Q_{i,sum,max}$ normalised to the number of events and ROCs.

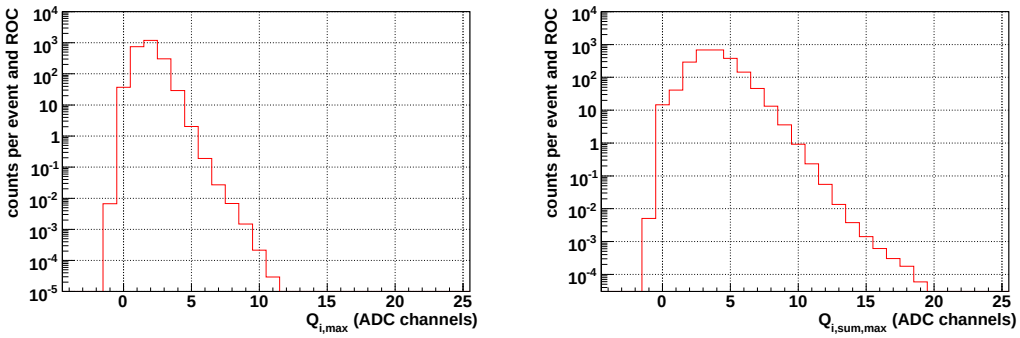

Figure 8.2: The distributions of $Q_{i,max}$ and $Q_{i,sum,max}$ in ADC channels above the baseline normalised to the number of events and ROCs. The data is taken with $U_A = 0\,\mathrm{V}$ and thus only the fluctuations around the baseline are recorded.

To achieve a purity of the recorded signal better than one noise pad per recorded event and ROC corresponding to less than one count in the histogram, T_{IS} has to be six ADC channels above baseline (compare left panel of figure 8.2). If T_{IS} is chosen to be nine ADC channels above baseline, less than one noise pad per event and 540 ROCs is recorded. This corresponds to a purity better than one noise pad per event in the whole TRD.
Analogous, a purity better than one noise pad per recorded event and ROC can be achieved with $T_{IT} = 10$ ADC channels above baseline (see right panel of figure 8.2), whereas a cluster threshold T_{IT} of fifteen ADC channels leads to a purity better than one

noise pad per event in the whole TRD. Since the amplification voltage U_A, which provides gas amplification, influences the noise behaviour of the pads, the noise distribution in data that have to be taken with $U_A > 0\,\mathrm{V}$ is expected to differ slightly from the one in figure 8.2.

Calibration of the Single Threshold T_{IS}

The danger arising from data compression is that information about particle tracks may get lost. To analyse the ratio of true hits that are kept to the total amount of true hits as a function of the thresholds used for ZS, the distributions of $Q_{i,max}$ and $Q_{i,sum,max}$ in ADC channels above baseline are investigated in $2 \cdot 10^4$ events taken at $U_A = 1500\,\mathrm{V}$ with a coincidence trigger. In figure 8.3, the results for $Q_{i,max}$ of all pads, which meet the condition in equation 8.2, are shown. The distribution is a superposition of the central pads of all true hits and an undefined amount of read out noise pads (left panel of figure 8.3) and it can be subdivided into two parts. The peak starting at $Q_{i,max} = 0\,\mathrm{ADC}$ channels above baseline mainly corresponds to noise pads, on which no charge was deposited by a primary particle. Therefore, the peak is called 'noise peak' in the following. The other part ('data peak') is the distribution of $Q_{i,max}$ of the central pads of all true hits. Since the distribution results from the fluctuations in energy loss of the charged primary particles passing through the ROC, the data peak can be fit with a Landau distribution [Lan44].
The peak in the region between 950 and 1023 ADC channels is due to digitisation effects. Output values of the PASA that correspond to ADC values higher than 1023 ADC channels result in an overflow and the return value of the ADC is set to 1023 ADC channels. Afterwards, the pedestal correction filter subtracts the mean value of the PASA output (see chapter 3.3.4), and that leads to the distribution of overflow values between 950 and 1023 ADC channels. Consequently, pads with more than 950 ADC channels in one time bin can lead to an erroneous position reconstruction and thus have to be cut out. If a lower voltage U_A is applied, this effect can be reduced.
In the region of overlap between the noise peak and the data peak, it is impossible to distinguish between $Q_{i,max}$ corresponding to noise pads and to true hits. Thus this region is the subject of further analysis to determine the effect of the ZS on the ratio of true hits kept to the total amount of hits.

To get the information how many central pads of true hits are rejected as a function of T_{IS}, the Landau distribution is determined, which corresponds to the distribution of $Q_{i,max}$ of the central pads of all true hits. The resulting Landau distribution with a most probable value of $Q_{i,max} = 90$ ADC channels above baseline and a sigma of 30 ADC channels is shown in the right panel in figure 8.3. The integral of the determined Landau distribution

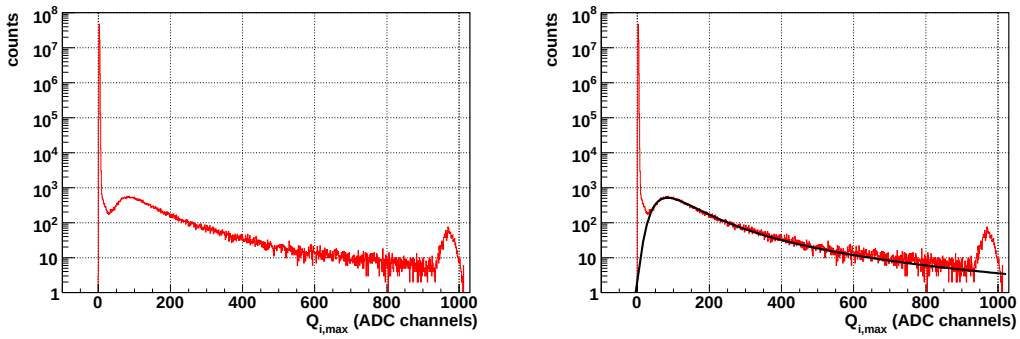

Figure 8.3: The results of a measurement with $U_A = 1500\,\mathrm{V}$. Left panel: The distribution of $Q_{i,max}$ in ADC channels above baseline of all pads, which fulfil the condition 8.2, is a superposition of the central pads of all true hits and an undefined amount of read out noise pads. Right panel: The data peak can be fit with a Landau distribution (black line).

over the interval [0,950] can be assigned to the amount of all true hits, whereas the integral over [0,T_{IS}] is the fraction lost by the usage of the applied threshold T_{IS}.
The fraction of the true hits that are kept as a function of T_{IS} is presented in figure 8.4.

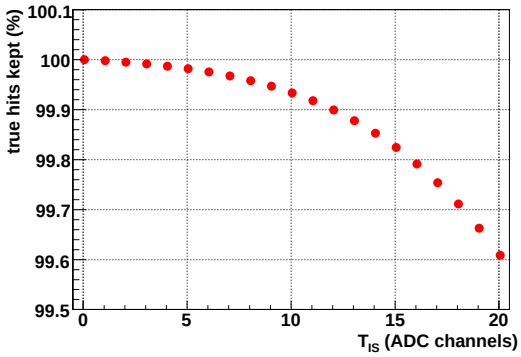

Figure 8.4: The ratio of the true hits kept to the total amount of true hits as a function of T_{IS}.

To obtain less than one noise pad for all 540 ROCs of the TRD ($T_{IS} = 9$ adc channel above baseline) the loss of central pads of all true hits will be 0.05 %, whereas a required purity better than one noise pad per event and ROC leads to a loss of 0.03 %.

Calibration of the Cluster Threshold T_{IT}

In the left panel of figure 8.5 the distribution of $Q_{i,sum,max}$ from a measurement with $U_A = 1500\,\mathrm{V}$ is presented. Analogous to the distribution of $Q_{i,max}$, this distribution of the central pads corresponds to noise superimposed with the distribution of $Q_{i,sum,max}$ of the central pads of true hits. The determined Landau distribution of the data peak has

a most probable value of $Q_{i,sum,max} = 142$ ADC channels above baseline and a sigma of 45 ADC channels and is shown in the right panel of figure 8.5. Since $Q_{i,sum,max}$ is a sum over three adjacent pads, the integral of the Landau distribution is calculated over the interval [0,3071] to get the total amount of true hits and over [0,T_{IT}] to get the amount of central pads of all true hits rejected.

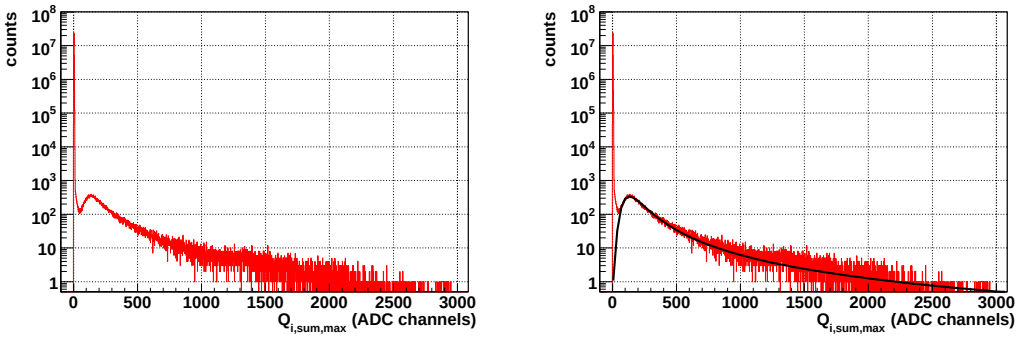

Figure 8.5: The results of a measurement with $U_A = 1500\,\mathrm{V}$. The distribution of $Q_{i,sum,max}$ in ADC channels above baseline of all pads, which fulfil the condition 8.2 (left panel). The distribution of those $Q_{i,sum,max}$, which corresponds to true hits, is a Landau distribution (right panel).

The resulting ratio of the true hits that are read out to the total amount of true hits is plotted in figure 8.6 as a function of the cluster threshold T_{IT}. If a purity better than one noise pad per event and ROC is required, the threshold has to be set to $T_{IT} = 10$ ADC channels above baseline. That leads to a loss of 0.014 % of the central pads of all true hits. The setting $T_{IT} = 15$ ADC channels above baseline, where less than one pad per event is recorded in the TRD, leads to a loss of 0.032 %.

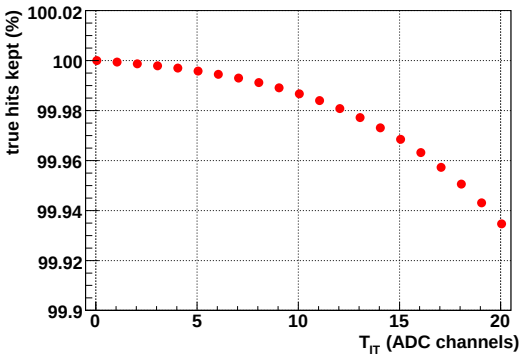

Figure 8.6: The ratio of the true hits kept to the total amount of true hits as a function of T_{IT}.

The effect of T_{IS} on the neighbouring pads

The central pads which satisfy equation 8.2 have two neighbours. Since these are needed for the position reconstruction, a further investigation of the effect of the ZS on the readout of the neighbouring pads is required. In the following, the neighbouring pad, which is of the higher or equal $Q_{i,max}$, is called the 'big neighbour', whereas the other one is called the 'small neighbour'. The distinction between them is necessary because the effect of the ZS on the former differs extremly from the effect on the latter.
The $Q_{i,max}$ distribution of the big neighbours is shown in the left panel of figure 8.7 and the resulting ratio of the big neighbours kept to the total amount of true hits is plotted in the right panel of figure 8.7. If T_{IS} is chosen to be six ADC channels above baseline, 0.67 % of the big neighbours are not marked to be read out. If a purity better than one noise pad per event in the TRD is required, the loss increases to 1.03 %.

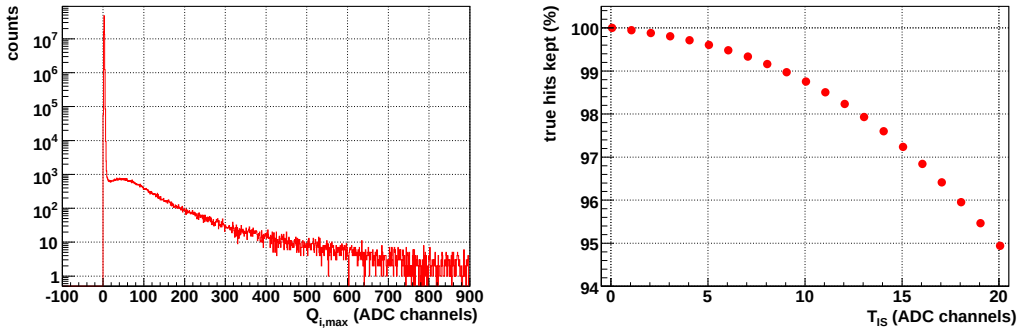

Figure 8.7: The distribution of $Q_{i,max}$ of the big neighbours (left). Analogue to the central pad the data peak is a Landau distribution, which can be used to calculate the loss ratio of the big neighbours of all true hits (right).

The $Q_{i,max}$ distribution of the small neighbours differs from the previous distributions since the noise peak and the data peak are no longer separable. This is shown in the left panel of figure 8.8. In the region of interest, the distribution of $Q_{i,max}$ can be fit approximately with a sixth-degree polynomial function (see upper right panel of 8.8). The fit has a high systematic uncertainty if it is extrapolated to the region of the noise peak. Thus the calculated ratio of small neighbours kept to the total amount of true hits is a rough estimation. It is presented in the lower panel of figure 8.8. The application of the threshold $T_{IS} = 6$ ADC channels above baseline leads to a loss of small neighbours of 31 % wheras with $T_{IS} = 9$ ADC channels above baseline the signal loss increases up to 41 % of the small neighbours.
Since $Q_{i,max}$ of the small neighbour takes the value of 1 adc channel below baseline, some small neighbours already will get lost if the threshold is set to the baseline value of 10 ADC channels. In that case almost the complete noise is read out as well and thus no

data compression is proceeded.

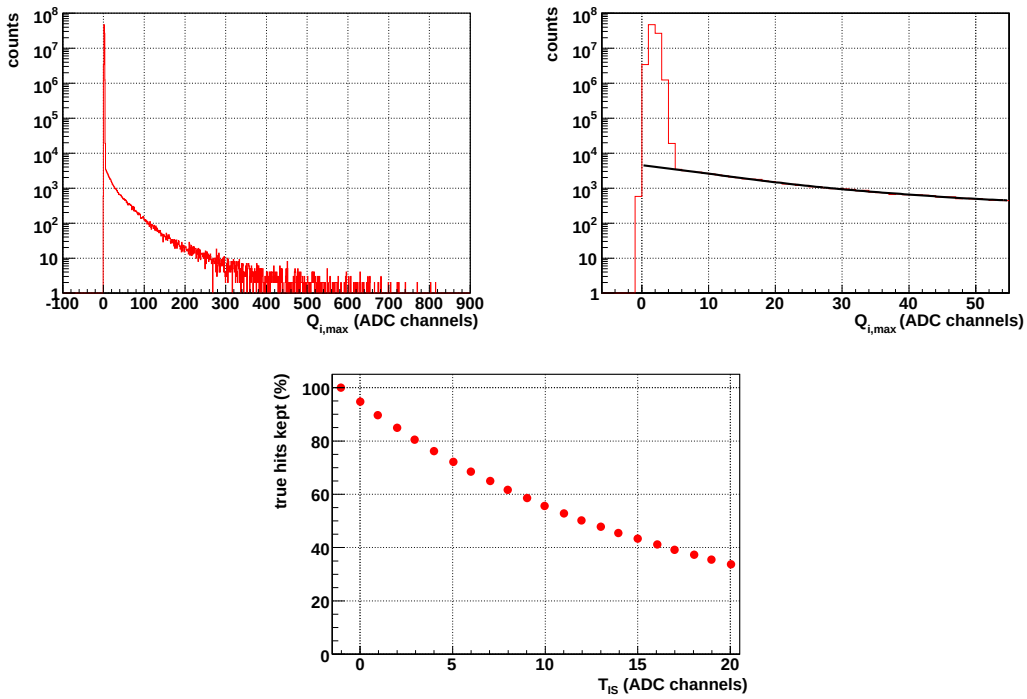

Figure 8.8: Upper left panel: The distribution of of $Q_{i,max}$ of the small neighbours differs from the distribution corresponding to the central pad and the big neighbour pad. Upper right panel: The data can approximately be fit with a sixth-order polynomial function. Lower panel: The calculated loss ratio of the small neighbour pads of all true hits.

The determined values for the thresholds T_{IS} and T_{IT} in this section correspond to a measurement with an anode voltage $U_A = 1500\,\mathrm{V}$ and a gas mixture in the chambers of Ar/CO_2 (84.6:15.4). They have to be recalibrated for other setups. In addition, these values are corresponding to data taken with by-passed tail cancellation filter, which influences the recorded distributions of $Q_{i,max}$ and $Q_{i,sum,max}$. The effect is investigated in section 8.2.1.

If the same purity is required, the application of the cluster threshold T_{IT} leads to smaller signal loss than the single threshold T_{IS} (see table 8.1). Therefore, the application of the cluster threshold T_{IT} is recommended.

	no-TC data			
	T_{IS} (ADC channels a. bl.*)		T_{IT} (ADC channels a. bl.)	
	6	9	10	15
purity	$<1\ \frac{\text{pad}}{\text{event}\cdot\text{ROC}}$	$<1\ \frac{\text{pad}}{\text{event}\cdot 540\cdot\text{ROC}}$	$<1\ \frac{\text{pad}}{\text{event}\cdot\text{ROC}}$	$<1\ \frac{\text{pad}}{\text{event}\cdot 540\cdot\text{ROC}}$
loss of central pads (%)	0.05	0.03	0.01	0.03

Table 8.1: Comparison of the the determined thresholds (* 'ADC channels above baseline') for data taken with by-passed TC filter and with applied TC. The anode voltage U_A is set to 1500 V and the gas mixture is Ar/CO_2 (84.6:15.4).

Effect of Zero Suppression on the Position Resolution

Since the neighbours are needed to calculate the position of the centre of a hit using the PRF, the influence of the ZS on the position resolution has to be investigated.
In addition to the set of three criteria for the ZS, the TRAP provides the so-called neighbour flag (n_{flag}). If the flag is set to zero, the two neighbours of each pad that reaches the threshold are marked to be read out as well. Figure 8.9 shows the position resolution as a function of T_{IS} (left panel) and T_{IT} (right panel). The black dots correspond to data taken with $n_{flag} = 0$ and the red squares correspond to $n_{flag} = 1$.

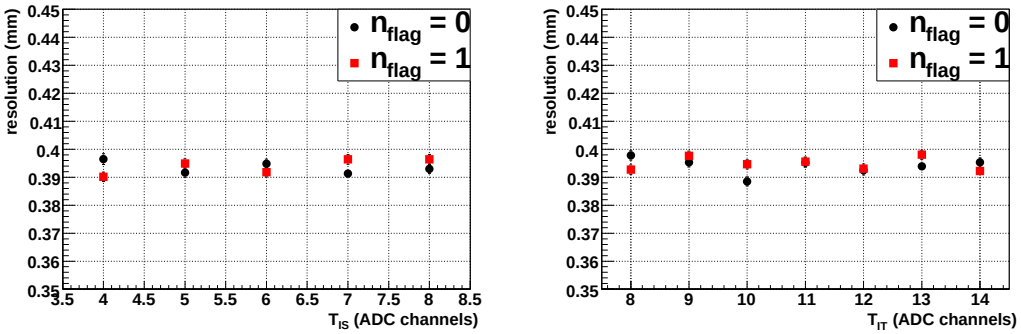

Figure 8.9: The position resolution in a L0-type ROC as a function of the single pad threshold T_{IS} (left) and the cluster pad threshold (right).

For T_{IS} as well as for T_{IT} the resolution remains constant for different thresholds. The large loss of the small neighbours has no noticeable effect on the resolution and hence the neighbour flag has no influence on the resolution either. An explanation for this is that the Gaussian PRF is already well-defined by two values of Q_i and Q_{i-1} or Q_i and Q_{i+1}. Thus the calculated displacement y does not have to be shifted due to the loss of the smaller neighbour. In equation 6.10 given for the calculation of y using 3-Pad-Clusters the displacement is a weighted average with the weights $w_1 = Q_{i-1}^2$ and $w_2 = Q_{i+1}^2$. Therefore, the term containing the big neighbour has a higher weight and the shift due to the term that contains the small neighbour is rather small. Consequently, the position resolution performance does not suffer from the loss of small neighbour pads.
It has to be kept in mind that for the purpose of reconstruction of energy deposition and particle identification using TR the information of all pads, on which charge is deposited is essential. Since the loss ratio of the small neighbours becomes significant at rather low values of T_{IS} and T_{IT}, the neighbour flag should be used in the experiment to obtain all deposited charge of the primary particle.

8.2 Effect of Zero Suppression on the Event Size

In the event buffer the decision is made which pads are marked to be read out, using the discussed set of criteria. The pad information including the position of the pads and their charge is called ‘raw data‘ and transferred to the GTU, where the raw data of each event from all ROCs of one SM is merged and shipped to storage.
The structure of the stored events includes several headers. Two of them are the ‘date header‘ (size: 68 bytes), which contains the total event size and the ‘GTU header‘ (size: 504 bytes). In addition, every MCM has its own header (4 bytes each) and a ‘channel mask‘ (4 bytes each). The MCM headers and the channel mask of one ROC in one event sum up to a total size of 1024 bytes, with the exception of ROCs in stack two that contain 32 MCMs less. For these the MCM headers and the channel masks sum up to 768 bytes. The channel mask provides the information about which pads of the corresponding MCM have been marked to be read out. In the case that at least one pad is marked, the mask is followed by 40 bytes of information per marked pad containing its sampled and filtered signal of all 30 time bins. Furthermore, there are two ‘half chamber headers‘ (8 bytes each) and the end markers of the merged and shipped tracklet information (‘tracklets‘) from the TPs (16 bytes). Altogether the headers, channel masks and tracklet information sum up to a value of 1620 bytes for an empty event with no marked pads. In the following, the 1620 bytes are subtracted from the event size so that an event with no marked pads has an effective size of zero bytes.
Once the reliability of the data structure in the read out stream is established, it is planed to decrease the total event size by writing MCM headers only if at least one corresponding pad is marked for read out.

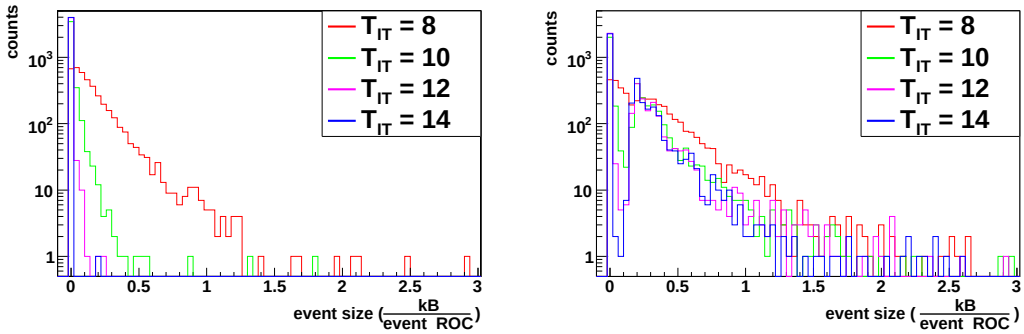

Figure 8.10: The distribution of the event size for different thresholds T_{IT} for $U_A = 0\,\mathrm{V}$ (left) and $U_A = 1500\,\mathrm{V}$ (right). The data is taken with the coincidence trigger.

Figure 8.10 shows the different distributions of event sizes corresponding to different cluster thresholds T_{IT}. The left panel shows the results of measurements with U_A set to 0 V so that all pads only show fluctuations around the baseline. With $T_{IT} = 8$ ADC channels

above baseline most events already have a size of zero bytes, but in some events several pads have been marked for readout. With $T_{IT} = 12$ ADC channels above baseline, an acceptable noise suppression is achieved (compare figure 8.2) and with $T_{IT} = 14$ ADC channels above baseline the noise is almost cut out completely.
The right panel of figure 8.10 shows the results of a measurement with U_A set to 1500 V. The ROCs are designed in a way that the signal created by a passing particle spreads over three pads on the average. In addition the particle generally has an incident angle $\alpha \neq 0°$ leading to a shift of the signal distribution on the adjacent pads in subsequent time bins and thus to the effect that in different time bins different pads reach the threshold to be read out in all 30 time bins. Hence it is expected that if a primary particle crosses the ROC, several adjacent pads are marked for readout. Recorded 1-pad-clusters and 2-pad-clusters have a high probability to originate from noise and therefore, the counts in the region from 0 bytes to 120 bytes decrease with increasing threshold. In addition true 1-pad-clusters and 2-pad-clusters correspond to ionisation processes of the primary particle with less than average deposited charge and are thus cut out at smaller thresholds than true 3-pad-clusters.

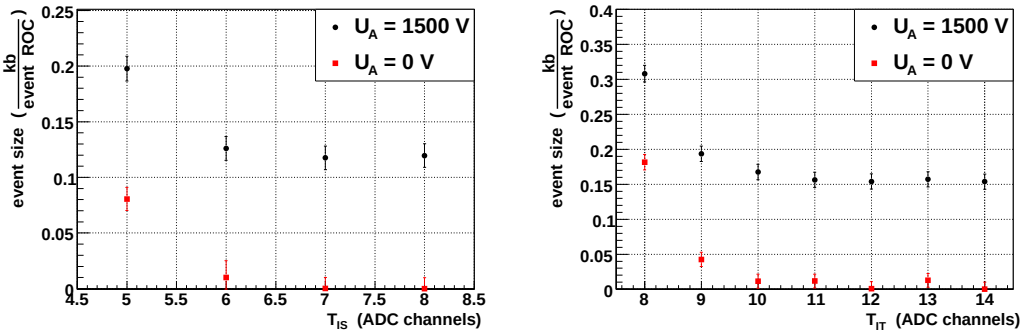

Figure 8.11: Size of events taken with $U_A = 0$ V and $U_A = 1500$ V as a function of T_{IS} (left) and T_{IT} (right). The neighbours have not been read out ($n_{flag} = 1$).

In figure 8.11, the average event size is presented as a function of T_{IS} and T_{IT}. Every data point corresponds to the average event size from a measurement with $2 \cdot 10^4$ events. The values $T_{IS} = 6$ ADC channels above baseline and $T_{IT} = 10$ ADC channels above baseline, which correspond to a required purity better than one noise pad per event and ROC (compare with figure 8.2), thus lead to an event size that is smaller than 40 bytes per event and ROC. Furthermore, the event size increases by less than 40 bytes per event and ROC in case of $U_A = 0$ V due to the neighbour flag being set to zero if the same threshold values are applied. That corresponds to less than one additional noise pad per event and ROC due to the use of the neighbour flag. This can be seen in figure 8.12, which shows the increase of the event size if the neighbours of marked pads are always read out ($n_{flag} = 0$).

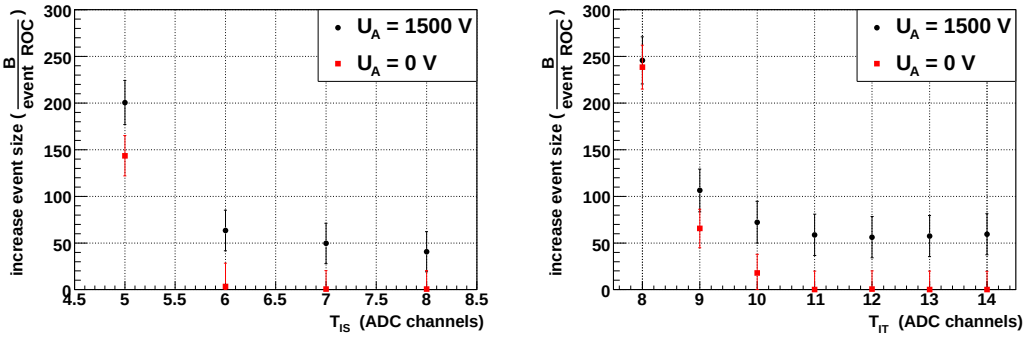

Figure 8.12: Increase of the event size, if neighbours are read out additionally ($n_{flag} = 0$) as a function of the threshold T_{IS} (left) and T_{IT} (right).

The condition which pads have to fulfil to be read out can be any logical combination of the critera offered by the TRAP. One example for such a combination is given by

$$I_{0,i}(tb) = \begin{cases} 0 & if \quad Q_{i,sum} \geq T_{IT} \quad \vee \quad Q_i \geq T_{IS} \ . \\ 1 & otherwise \end{cases} \tag{8.3}$$

In the left panel of figure 8.13, the average event size as a function of the tuple (T_{IS}, T_{IT}) is presented for a measurement with $U_A = 0\,\mathrm{V}$. It can be achieved that in one ROC less than one pad is read out per event due to noise if T_{IS} is chosen to be ≥ 6 ADC channels above baseline and T_{IT} is chosen to be ≥ 10 ADC channels above baseline. A chosen requirement that a pad is read out if it reaches $T_{IS} = 6$ ADC channels above baseline or $T_{IT} = 10$ ADC channels above baseline leads to an event size of 19.2 bytes per event and ROC. The application of the single threshold $T_{IS} = 6$ ADC channels above baseline without further requirements leads to an event size of 10.0 bytes per event and ROC and the application of the cluster threshold $T_{IT} = 10$ ADC channels above baseline without further requirements leads to an event size of 11.5 bytes per event and ROC. A comparison between the sum of the event sizes, if both thresholds are applied separately, of 21.5 bytes per event and ROC, and the event size resulting from the condition in equation 8.3 of 19.2 bytes per event and ROC leads to the assumption that the two thresholds cut out two different sets of noise pads. Hence a better noise suppression is expected if pads have to reach the cluster threshold and the single threshold to be read out. The resulting event sizes and the effect on the signal loss have to be investigated in the future.
The right panel of figure 8.13 shows the increase of the event size if the neighbour flag is set to zero. The setting $T_{IS} = 6$ ADC channels above baseline and $T_{IT} = 10$ ADC channels above baseline leads to an increase of the event size of 26.5 byte per event and ROC.

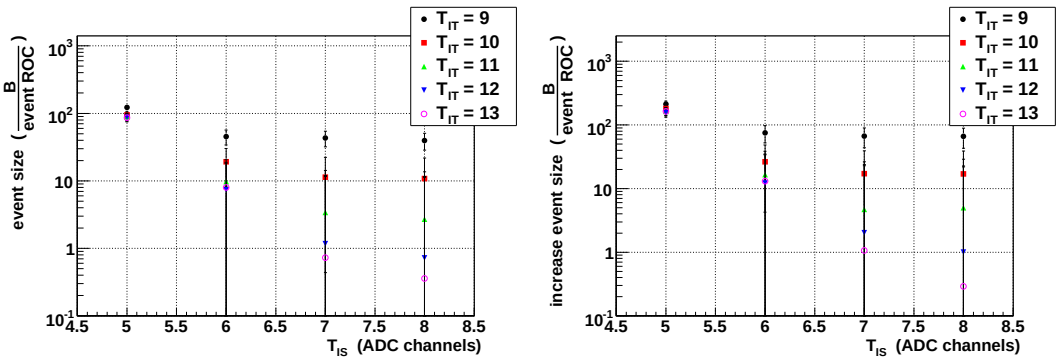

Figure 8.13: Left: Event size as a function of the combination of T_{IS} and T_{IT}. The pads are read out if they reach T_{IS} or T_{IT}. Right: Increase of the event size, if neighbours are read out additionally.

8.2.1 Effect of Tail Cancellation on the Efficiency of Zero Suppression

Simulations of the digital filter in the TRAP have shown that the tail cancellation filter influences the recorded fluctuations around the baseline and thus the RMS of the noise in ADC channels increases by 10 % [Kal09]. In figure 8.14, the average RMS of the noise of ten events is presented for data taken without TC (left panel) and with TC (right panel). The same TC parameters are applied that are given in equation 6.15. Futhermore, the tail cancellation filter subtracts that part of the signal, which is due to ion tails and thus leads to smaller values of $Q_{i,max}$ and $Q_{i,sum,max}$. Due to the fact that the signal is filtered first and afterwards stored in the event buffer where the ZS is applied, the TC has an influnce on the efficiency of the ZS.

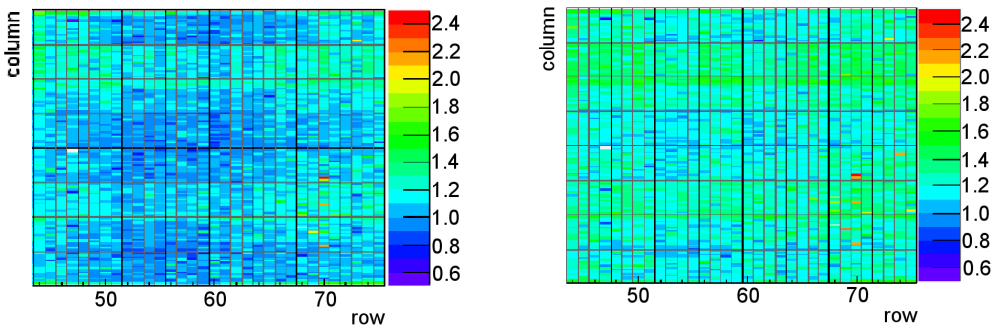

Figure 8.14: Average RMS of the fluctuations around the baseline in ADC channels of ten events taken without TC (left) and with TC (right) in stack three and four of layer one.

In figure 8.15 the resulting distributions of $Q_{i,max}$ and $Q_{i,sum,max}$ normalised to the number of events and ROCs originating from TC data are compared with the distributions of $Q_{i,max}$ and $Q_{i,sum,max}$ from no-TC data. Both data sets are taken with $U_A = 0\,\mathrm{V}$. The distributions of $Q_{i,max}$ and $Q_{i,sum,max}$ differ strongly from the distributions originating from data taken without TC.

To achieve a purity of one noise pad per event in 540 ROCs the single cluster threshold has to be chosen as $T_{IS} = 12$ ADC channels above baseline compared with the value $T_{IS} = 9$ ADC channels above baseline for measurements with by-passed tail cancellation filter (compare chapter 8.1). In the case of the cluster threshold the value increases from $T_{IT} = 15$ to $T_{IT} = 18$ ADC channels above baseline.

For a purity better than one noise pad per event and ROC the value of T_{IS} stays the same ($T_{IS} = 6$ ADC channels above baseline) as for no-TC data. T_{IT} needs to be increased in that case from ten to eleven ADC channels above baseline. Figure 8.16 shows the average event sizes of TC and no-TC data as a function of T_{IS} and T_{IT}. Each data point

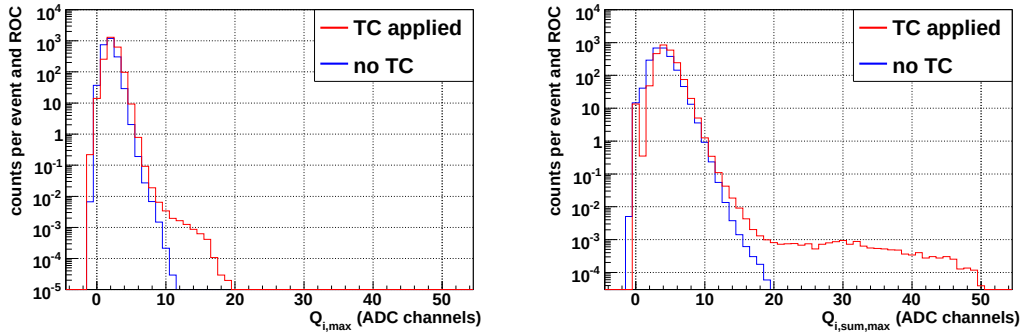

Figure 8.15: The normalised distributions of $Q_{i,max}$ and $Q_{i,sum,max}$ in ADC channels above the baseline. The data is taken with tail cancellation and $U_A = 0\,\mathrm{V}$ (red line). The distributions differ extremly from the previous ones (see chapter 8.1), which are taken without TC (blue line).

corresponds to the average event size of a measurement with $2 \cdot 10^4$ events. U_A is set to 0 V and the neighbours have been read out for all marked pads ($n_{flag} = 0$). Since the RMS of the noise is higher, the event size at certain thresholds of the filtered data compared with the data taken without TC increases, especially in the case of low threshold values.

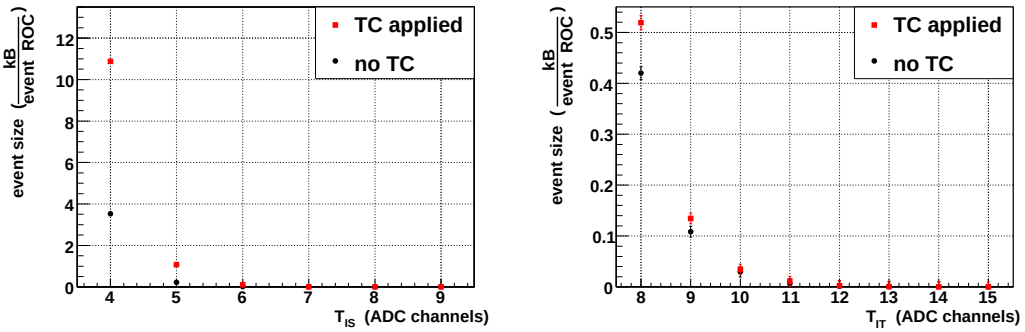

Figure 8.16: The size of events taken with TC as a function of the single threshold T_{IS} (left) and the cluster threshold T_{IT} (right).

To study the effect of the data compression by ZS on data that is taken with TC the distributions of $Q_{i,max}$ and $Q_{i,sum,max}$ are analysed. The data peak can again be approximated with a Landau distribution (see left panels in figure 8.17). The parameters of the Landau distributions are given in table 8.2. Since the average signal decreases due to TC, which subtracts the contribution of the tails to the signal, the most probable value of $Q_{i,max}$ and $Q_{i,sum,max}$ decreases as well compared with the values corresponding to no-TC data.

The resulting ratio of true hits that are kept to the total amount of true hits is presented in the right panels of figure 8.17. If a noise suppression better than one pad per event and

	$Q_{i,max}$ (ADC channels a. bl.*)		$Q_{i,sum,max}$(ADC channels a. bl.)	
	no-TC data	TC data	no-TC data	TC data
most probable value	90.4	68.7	142.2	111.7
σ	30.0	26.5	45.2	39.4

Table 8.2: Parameters of the Landau distributions of $Q_{i,max}$ and $Q_{i,sum,max}$ (* 'ADC channels above baseline'). The values are given for $U_A = 1500$ V and a gas mixture of Ar/CO_2 (84.6:15.4).

ROC is intended, the loss of the central pads of all true hits is 0.25 % for $T_{IS} = 6$ ADC channels above baseline and 0.12 % for $T_{IT} = 11$ ADC channels above baseline.

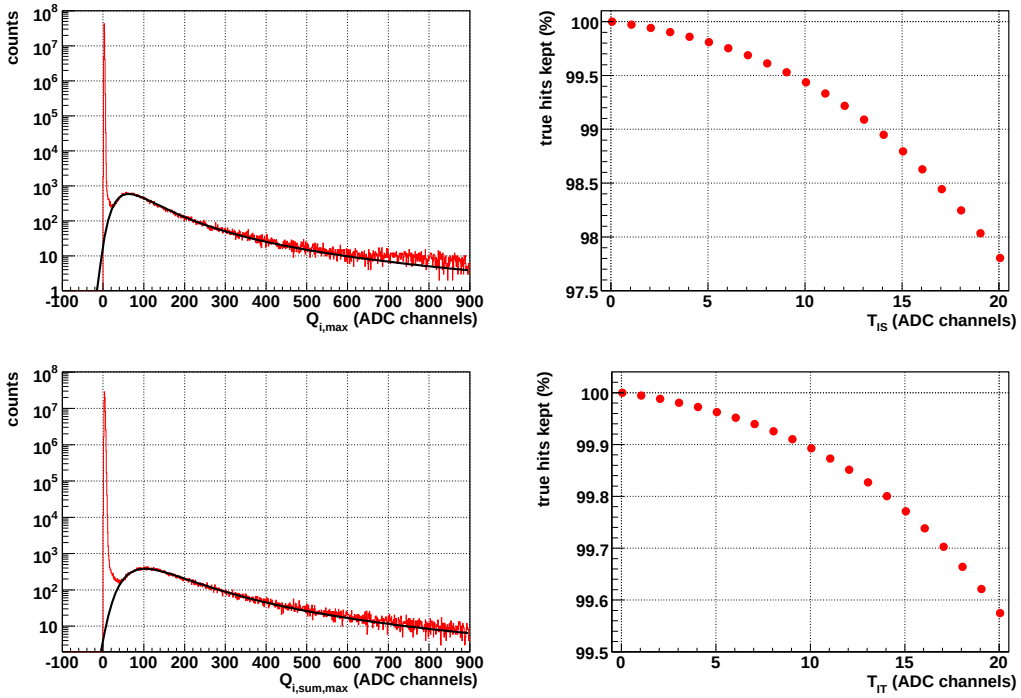

Figure 8.17: The distributions of $Q_{i,max}$ and $Q_{i,sum,max}$ of data taken with TC (left panels) and the resulting ratios of the central pads of true hits kept to the total amount of true hits (right panels).

The signal loss of the two neighbouring pads as a function of the applied single threshold T_{IS} is presented in figure 8.18. If a purity better than one noise pad per event and ROC is required, the single threshold $T_{IS} = 6$ ADC channels above baseline will lead to a loss of the big neighbours of 2.5 % and a loss of 35 % of the small neighbours.
If TC is applied, $Q_{i,max}$ of both neighbouring pads take the value of 1 adc channel below baseline. Thus some of the neighbouring pads will already get lost if the threshold T_{IS} is

set to the baseline value that is ten ADC channels.

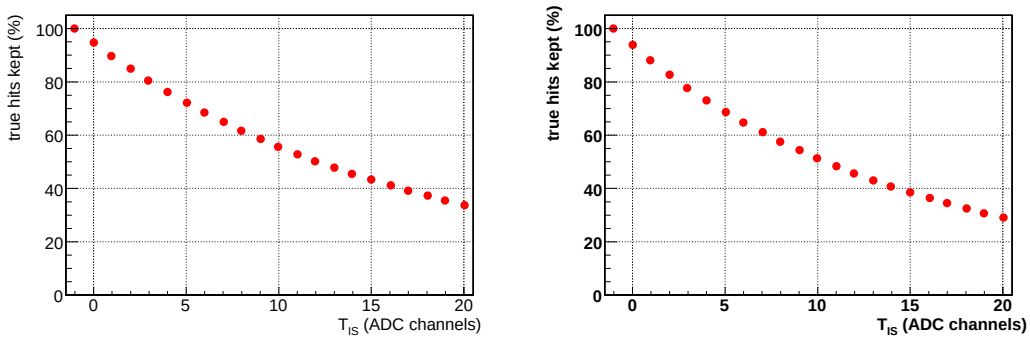

Figure 8.18: The ratios of the big neighbours (left panel) and the small neighbours (right panel) of true hits kept to the total amount of true hits.

In the table 8.3 the obtained values for T_{IS} and T_{IT} to reach a certain purity for data taken with applied TC is presented. A comparison with the data taken with by-passed tail cancellation filter (see table 8.1) shows that the increased noise and the decreased signal of data taken with tail cancellation filter lead to a higher loss of true hits if the same purity is required.

	TC applied			
	T_{IS} (ADC channels a. bl.*)		T_{IT} (ADC channels a. bl.)	
	6	12	11	18
purity	$<1\ \frac{\text{pad}}{\text{event}\cdot\text{ROC}}$	$<1\ \frac{\text{pad}}{\text{event}\cdot 540\cdot\text{ROC}}$	$<1\ \frac{\text{pad}}{\text{event}\cdot\text{ROC}}$	$<1\ \frac{\text{pad}}{\text{event}\cdot 540\cdot\text{ROC}}$
loss of central pads (%)	0.25	0.80	0.12	0.34

Table 8.3: Comparison of the the determined thresholds (* 'ADC channels above baseline') for data taken with by-passed TC filter and with applied TC. The anode voltage U_A is set to 1500 V and the gas mixture is Ar/CO_2 (84.6:15.4).

CHAPTER 9

Summary

The ALICE experiment at the LHC at CERN is a dedicated heavy ion experiment. It will study strongly interacting matter in ultrarelativistic heavy ion-collisions to explore the QCD phase diagram of nuclear matter. ALICE consists of several detectors one of them being the TRD that provides particle tracking and electron identification.
In this diploma thesis the position resolution performance of the Multi Wire Proportional Chambers of the TRD has been examined using cosmic rays in a dedicated trigger setup. The position resolution is an approximately linear function of the pad width of the six different ROC-types and it decreases with larger incident angles of the primary particle. Averaged over all incident angles the position resolution takes values between 389 μm in case of a L0-typer ROC and 418 μm for a L5-type ROC.
The TRD provides a trigger decision, which is based on the detection of particles with high transverse momentum and the identification of electrons. Therefore, particle tracks have to be recognised and the calculation of the track segments in the chambers have to be performed online in a certain time. That is done in the TRAP chip, which is a part of the TRD front-end electronics.
Parameters needed for the purpose of online position reconstruction in the TRAP have been calibrated for all six different chamber types. Furthermore, a quality cut to avoid the consideration of multiple hits with superpositioned signal distributions leading to erroneous position reconstruction has been calibrated.
In addition to the calculated track parameters and the electron probability, part of the recorded raw data of the events is read out and stored as well. During the event the whole raw data is stored in the event buffer of the TRAP, where the decision is made which pads might carry a part of a true hit and whose recorded signal thus is shipped to storage. Therefore, the two thresholds T_{IS} and T_{IT} are employed that the signal of a single pad and of three adjacent pads respectively have to reach. A method for calibration of these

thresholds has been studied, to provide a good data compression by noise suppression and to minimise the caused signal loss.
The obtained values correspond to a measurement with an anode voltage $U_A = 1500\,\mathrm{V}$ and a gas mixture in the chambers of Ar/CO_2 (84.6:15.4) and thus have to be recalibrated for the usage in the experiment with a different gas mixture and a variant anode voltage. If a certain purity of the data is required, the application of the cluster threshold T_{IT} leads to less signal loss compared to the usage of the single threshold T_{IS}. But as the two thresholds cut out two different sets of noise pads, a combinated requirement is recommended, where both thresholds have to be reached by a pad that is marked for readout.

List of Figures

Bibliography

[A+04] A. Andronic et al. Electron identification performance with ALICE TRD prototypes. *Nucl. Instr. and Meth. Phys. Res. A*, 552:40–44, 2004.

[A+05] V. Angelov et al. ALICE TRAP user manual, 2005. revision 1.1.

[A+08] C. Amstel et al. Particle Physics Booklet 2008, December 18, 2008.

[atp08] ALICE technical paper I: ALICE experiment at the CERN LHC, 2008.

[Bat07] B. Bathen. Aufbau eines Triggers für Tests der ALICE-TRD-Supermodule mit kosmischer Strahlung. diploma thesis, 2007. Institut für Kernphysik Universität Münster.

[Bat09] B. Bathen. personal communication, 2009.

[Bia99] S. Biaggi. *Nucl. Inst. Meth.*, A421:234, 1999.

[BMS07] P. Braun-Munziger and J. Stachel. The quest for the quark gluon plasma. *Nature*, 448:302–309, 2007.

[BR94] W. Blum and L. Rolandi. *Particle Detection with Drift Chambers.* Springer, 1994.

[BRR08] W. Blum, W. Riegler, and L. Rolandi. *Particle Detection with Drift Chambers, 2nd edition.* Springer, 2008.

[Bus02] O. Busch. Position resolution with prototypes of ALICE transition radiation detector. diploma thesis, 2002. Gesellschaft für Schwerionenforschung, Darmstadt.

[cer09] http://aliceinfo.cern.ch, 2009.

[dC03] J. de Cuveland. Entwicklung der globalen Spurrekonstruktionseinheit für den ALICE Übergangsstrahlungsdetektor am LHC (CERN). diploma thesis, 2003. Fakultät für Physik und Astronomie Universität Heidelberg.

[Ems05] D. Emschermann. The geometry of the TRD padplane. http://www.physi.uni-heidelberg.de/demscher/alice/padplane/, 2005.

[G+79] E. Gatti et al. Optimum geometry for strip cathode or grids in MWPC for avalanvhe localization along the anode wires. *Nucl. Instr. Meth. Phys. Res*, A 163:83–92, 1979.

[GF45] V. Ginzburg and I. Frank. Radiation of an uniformly moving electron due to its transition from one medium to another. *Journal of Physics, Moscow*, 9(5):353–362, 1945.

[GO05] J. F. Grosse-Oetringhaus. Physics performance of the ALICE central barrel using a distributed GRID computing environment. diploma thesis, 2005. Institut für Kernphysik Universität Münster.

[Gor00] M. I. Gorenstein. Quark-gluon plasma signatures in nucleus-nucleus collisions at CERN SPS. Invited Talk at Symposium on Fundamental Issues in Elementary Matter, 2000. arXiv:hep-ph/0011304v2.

[Gro08] Communication Group. LHC - the guide. CERN-Brochure-2008-001-Eng, 2008.

[Gut02] M. Gutfleisch. Digitales Frontend und Preprozessor im TRAP1-Chip des TRD-Triggers für das ALICE-Experiment am LHC. diploma thesis, 2002. Fakultät für Physik und Astronomie Universität Heidelberg.

[Gut06] M. Gutfleisch. Local signal processing of the ALICE transitian radiation detector at LHC (CERN). dissertation, 2006. Fakultät für Physik und Astronomie Universität Heidelberg.

[HM96] J. W. Harris and B. Müller. The search for the quark-gluon plasma. *Ann. Rev. Nucl. Part. Sci.*, 46:71, 1996.

[Kal09] M. Kalisky. personal communication, 2009.

[KB04] M. Klein-Bösing. Aufbau und Inbetriebnahme einer Funkenkammer. diploma thesis, 2004. Institut für Kernphysik Universität Münster.

[Kle08] J. Klein. Commisioning of and preparations for physics with the transition radiation detector in a large ion collider experiment at CERN. diploma thesis, 2008. Faculty of Physics and Astronomy University of Heidelberg.

[Lan44] L. Landau. *J. Phys. (USSR)*, 8:201, 1944. (Collected Papers, ed. D. ter Pergamon, Press, Oxford, q965).

[lhc95] The Large Hadron Collider: Conceptual design., 1995. CERN-AC-95-05-LHC.

[MG84] E. Mathieson and J. S. Gordon. Cathode charge distribution in multiwire chambers, II. Approximated and empirical formula. *Nucl. Instr. Meth. Phys. Res*, A 227:277–276, 1984.

[Per00] D. H. Perkins. *Introduction to High Energy Physics*. Cambridge University Press, 2000.

[ppr04] ALICE: Physics Performance Report, Volume i. *J. Phys. G: Nucl. Part. Phys.*, 30:1517–1763, 2004.

[Ros03] L. Rossi. The LHC superconducting magnets. Particle Accelerator Conference, 2003. PAC 2003. Proceedings of the Volume 1, pages 141–145, 2003.

[Sat90] H. Satz. Color screening and quark deconfinement in nuclear collisions. *Adv. Ser. Direct. High Energy Phys.*, 6:593, 1990.

[Sch02] H. Schmidt. Status and prospects of the CERN-LHC experimennt ALICE. *Acta Physica Polonica B*, 33(6):1651–1670, 2002.

[SM86] H. Satz and T. Matsui. j/ψ suppression by quark-gluon plasme formation. *Phys. Lett.*, B 178:416–422, 1986.

[Swo] S. Swordy. apod.nasa.gov/apod/ap060814.html. U. Chicago, NASA.

[tdr01] ALICE Technical Design Report of the Transition Radiation Detector, 2001. http://www-alice.gsi.de/trd/tdr/index.html.

[Vee98] R. Veenhof. *Nucl. Inst. Meth.*, A419:726, 1998.

[Web] H. Weber. http://th.physik.uni-frankfurt.de/7Eweber/weber.html.

[Wil09] A. Wilk. dissertation, 2009. Institut für Kernphysik Universität Münster.

[Won94] C. Y. Wong. *Introduction to High-Energy Heavy-Ion Collisions*. World Scientific Publishing Co. Pte. Ltd, 1994.

[Y$^+$06] W. M. Yao et al. Review of particle physics. *J. Phys. G: Nucl. Part. Phys.*, 33:1–1232, 2006. 10.1088/0954-3899/33/1/001.

APPENDIX A

Danksagung

An dieser Stelle möchte ich mich bei den vielen Personen bedanken, die zum gelingen dieser Arbeit beigetragen haben.
Herrn Prof. Dr. Johannes P. Wessels danke ich für die interessante Aufgabenstellung, die Möglichkeit der Teilnahme an der DPG-Tagung in Darmstadt 2008 und den lehrreichen Aufenthalt am CERN 2007. Vor allem aber möchte ich danken für die Möglichkeit, am Aufbau eines Jahrhunderts-Experiments teilzuhaben.

Für die Betreuung dieser Arbeit und die geduldige Beantwortung sehr vieler Fragen bedanke ich mich bei Dr. Thomas Dietel.

Bei Melanie Klein-Bösing möchte ich mich bedanken für die ständige Diskussionsbereitschaft und viele interessante Anregungen.

Dr. Anton Andronic, Dr. Venelin Angelov und Dr. Bogdan Vulpescu danke ich sehr für die ausführliche Beantwortung vieler Fragen, sowie David Emschermann für den regen Informationsaustausch.

Der Münster-Main-Control-Crew danke ich für die gemeinschaftliche Bewältigung vieler Aufgaben und ein tolles Laborklima: Björn Albrecht, Helmut Baumeister, Dr. Thomas Dietel, Henriette Gatz, Helge Grimm, Markus Heide, Norbert Heine, Markus Rammler, Eva "Sveva" Sicking, Markus Tegeder, Wolfgang Verhoeven, Matthias Walter und Uwe Westerhoff . Für die angenehme Zusammenarbeit während der gesamten Zeit möchte ich mich auch bei den anderen Mitgliedern der Arbeitsgruppe bedanken: Christoph Baumann, Cyrano Bergmann, Holger Gottschlag, Sebastian Klamor, Christian Klein-Bösing, Melanie Klein-Bösing, Stefan Korsten, Michael Kowalik, Dr. Klaus Reygers, Baldo Sahlmüller,

Prof. Dr. Rainer Santo, Don Vernekohl, und Prof. Dr. Johannes P. Wessels.

Für die kritische Durchsicht der Arbeit and stilistische Anregungen möchte ich mich bedanken bei: Bastian Bathen, Melanie Klein-Bösing, Christian Klein-Bösing, Joachim Bokeloh und Karen Hugenberg (auch für den Pizza Dienst), Dr. Thomas Dietel, Christiane Ludwig, Baldo Sahlmüller, Dr. Anke B. Schmidt, Alexander Wilk, Kathrin Wulff und Michael Zacher.

Meinen Eltern danke ich für die große Unterstützung während des gesamten Studiums.

Und ich danke Simon, der in einem meiner Plots doch noch einen verschluckten Elefanten entdeckt hat.

Eigenständigkeitserklärung

Ich versichere, diese Arbeit selbständig verfasst und keine anderen als die angegebenen Hilfsmittel und Quellen benutzt zu haben.
Münster, 02. Februar 2009

Elke Svenja Wulff